DOKUZ EYLUL UNIVERSITY

GRADUATE SCHOOL OF NATURAL AND APPLIED

SCIENCES

PRODUCTION OF BaMeO$_3$ DOPED YBCO SUPERCONDUCTING THIN FILMS BY TFA-MOD TECHNIQUE

by

Murat BEKTAŞ

October, 2012

İZMİR

PRODUCTION OF BaMeO$_3$ DOPED YBCO SUPERCONDUCTING THIN FILMS BY TFA MOD TECHNIQUE
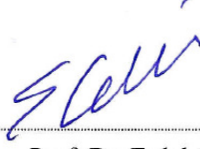
A Thesis Submitted to the
Graduate School of Natural and Applied Sciences of Dokuz Eylul University
In Partial Fulfillment of the Requirements for the Degree of Master of
Science in Metallurgical and Materials Engineering, Metallurgical and
Materials Program

by
Murat BEKTAŞ

October, 2012
İZMİR

ACKNOWLEDGEMENTS

PRODUCTION OF BaMeO₃ DOPED YBCO SUPERCONDUCTING THIN FILMS BY TFA MOD TECHNIQUE

ABSTRACT

High temperature superconducting materials (HTS) possess very high critical density (J_c) values at low temperature and magnetic fields. In these kinds of studies, crystalline defects, such as fine precipitates of non-superconducting phases, dislocations, vacancies, grain boundaries, twin boundaries, antiphase boundaries and insulating regions in grain boundaries are considered to act as pinning centers. However, the J_c values rapidly decrease with increasing temperature in magnetic field. The main reasons of the J_c depression are recognized to be the intrinsic crystalline anisotropy of HTS and the thermal fluctuations. Nevertheless, the lack of effective pinning centers should be noted as one of the main reasons. Depending on these reasons, a novel technology has been developed by means of a nanostructure engineering to create artificial pinning centers in HTS materials. In this respect, increasing critical current density and improvement of flux pinning properties of $YBa_2Cu_3O_{6.57}$ (YBCO) superconducting films with $BaMeO_3$ (Me: Zr, Hf, Ir, Sn, Mn, Mo, Nb etc.) perovskite nanodots, nanorods or nanoparticles, as pinning centers, on $SrTiO_3$ substrate are aimed using TFA-MOD method in this study.

Keywords: Flux pinning, superconductivity, thin film, YBCO

BaMeO$_3$ KATKILI YBCO SÜPERİLETKEN İNCE FİLMLERİN TFA-MOD TEKNİĞİ İLE ÜRETİLMESİ

ÖZ

Yüksek sıcaklık süperiletken malzemeleri (HTS) düşük sıcaklık ve yüksek manyetik alanlarda çok yüksek kritik akım yoğunluk (J_c) değerlerine sahiptir. Bu çeşit çalışmalarda süperiletken olmayan fazların nanoboyutta çökeltileri, dislokasyonlar, boşluklar, tane sınırları, ikiz sınırları, antifaz sınırları ve tane sınırlarındaki yalıtkan sınırlar gibi kristal hatalar akı iğnelemesi merkezleri olarak düşünülmektedir. Ancak J_c değerleri manyetik alanda artan sıcaklıkla hızlı bir şekilde düşmektedir. J_c'nin düşmesinin ana sebepleri yüksek sıcaklık süperiletkenlerinin intrinsik kristal anizotropisi ve termal dalgalanmalar olduğu bilinmektedir. Ancak, efektif iğnelenme merkezlerinin yok olması ana sebeplerden biri olarak not edilmelidir. Bu nedenlere bağlı olarak yeni teknoloji HTS malzemelerde yapısal iğnelenme merkezleri nanoyapılı mühendislik ile geliştirilmektedir. Bunu sağlamak amacıyla bu çalışmada TFA-MOD metodu kullanılarak, yapısal iğnelenme merkezleri olarak BaMeO$_3$ (Me: Zr, Hf, Ir, Sn, Mn, Mo, Nb vs.) perovskit yapılı nanonoktalar, nanoçubuklar veya nanopartiküller şeklinde yapıların YBa$_2$Cu$_3$O$_{6.57}$ (YBCO) süperiletken filmlerin içine ilave edilerek kritik akım yoğunluğunun artırılması ve akı iğnelenmesi özelliklerin geliştirilmesi hedeflenmiştir.

Anahtar sözcükler: Akı iğneleme, süperiletkenlik, ince film, YBCO.

CONTENTS

CHAPTER ONE
INTRODUCTION

1.1 Overview

Heike Kamerlingh Onnes discovered superconductivity in 1911. After that discovery, it has been a dream of scientists and engineers to use superconducting materials to build generators, transformers, motors, electrical circuits or wires. For more than 75 years these ideas had to remain a dream far from any commercial relevance since superconductivity only occurred at very low temperatures. The situation changed completely in 1986, when Bednorz and Müller found superconductivity in the system La-Ba-Cu-O at a relatively high temperature 35 K (Apetrii, 2009). Once the barrier was broken, hundreds of scientists tried various chemical compounds to get highest critical transition temperature (T_c). In March 1987, the compound $YBa_2Cu_3O_{7-x}$ (yttrium barium copper oxide, YBCO) took center stage, because of its high value of T_c=92 K. Subsequently, attention was focused on copper oxides, and before long the compound bismuth lead strontium calcium copper oxide was found with T_c= 105 K. In 1988 thallium barium calcium copper oxide was discovered with T_c = 125 K. After five years later the mercury compounds boosted the T_c record to 133 K. Under extremely high pressure, T_c can be increased over 150 K (Sheahen, 2002).

YBCO is one of the most widely studied high temperature superconductor, because of its promising and attractive aspects of applications, which include energy storage systems, current limiters, magnetic bearings, etc., above liquid nitrogen temperature (77 K) (Jha & Khare, 2010).

Generally, buffer and YBCO layers can be prepared using several deposition methods including physical deposition techniques, pulsed laser deposition (PLD), sputtering, thermal and e-beam evaporation and chemical deposition techniques like chemical vapor deposition and chemical solution deposition (CSD) (Knoth et al., 2007). CSD film fabrication can be grouped as sol-gel process and metal organic

deposition (MOD) techniques. The sol-gel technique is a low temperature method to synthesize materials. These materials are totally inorganic in nature or composed of inorganic and organics. This process can produce thin bond coating to provide excellent adhesion between the metallic substrate and the top coat. Resultant products have high homogeneity and purity (Kayatekin, 2006). Trifluoroacetates metal organic deposition method (TFA-MOD) is one of the most hopeful method to fabricate long-length YBCO tapes with high performance at low cost, In this method, trifluoroacetates, salts of yttrium, barium and copper is using as a starting solution (Nakaoka et al., 2009).

In TFA-MOD, during the calcination and firing processes water vapor and HF gas generated. They cause some chemical reactions with the substrate and buffer layers. Superconducting properties of final YBCO film is destroyed in terms of these reactions. Therefore, an appropriate buffer layer is essential for TFA-MOD. Alkaline and alkaline earth oxides (groups IA and IIA in the periodic table) react with HF gas during firing process. For instance, YBCO film can form on $LaAlO_3$ or $SrTiO_3$ substrate but cannot on MgO substrate (Araki & Hirabayashi, 2003).

High value of critical current density (J_c) even at higher applied magnetic fields is desired. To increase the value of J_c, the flux line lattice needs to be strongly pinned by various crystal imperfections and the pinning force density has to be large. Recently, several efforts have been performed to improve the pinning efficiency in YBCO system by chemical doping and introducing non-superconducting secondary phases (Jha & Khare, 2010).

Many groups have investigated so far the formation of effective pinning centers in YBCO layers prepared by pulsed laser deposition (PLD) methods. Their main focus has been the enhancement of intragrain pinning either through structural variations in mixed rare earth films or through the introduction of nanosized inclusions such as $BaIrO_3$, $BaHfO_3$, Y_2BaCuO_5, $BaZrO_3$ and Y_2O_3. In these experiments very promising results such as strongly improved critical current densities and enhanced irreversibility fields were presented (Engel, Thersleff, Hühne, Schultz & Holzapfel,

2007). In recent years, the issue of improving the effective pinning of magnetic flux lines in high temperature superconductor (HTS) films has been mostly studied (Aytug et al., 2010). $BaZrO_3$ (BZO) nanoparticles in YBCO thin films are one of the most popular ones which can prevent the vortex motion at high fields. Birlik, Erbe, Freudenberg, Celik, Schultz and Holzapfel (2010) have performed undoped and BZO doped YBCO thin films with CSD method. However, there are not much study about $BaIrO_3$ and $BaHfO_3$ acting as articial pinning centers.

1.2 Organization of The Thesis

In this study, we fabricated $BaMeO_3$ (Me: Hf and Ir) doped YBCO superconducting thin films by TFA-MOD method. Characterization of YBCO solutions were performed by measuring contact angle, viscosity and modulus. In order to use suitable process regime, Differential Thermal Analysis-Thermogravimetry (DTA-TG) and Fourier Transform Infrared (FTIR) devices were used to define chemical structure and reaction type of intermediate temperature products in the film production. The structural characterization of the samples was performed through X-ray diffractometer (XRD). Surface chemistry of thin films was investigated by X-Ray Photoelectron Spectroscopy (XPS). Surface morphology of the films was investigated by means of Scanning Electron Microscopy/Energy Dispersive Spectroscopy (SEM/EDS) and Atomic Force Microscope (AFM). The critical transition temperature (T_c) and critical current densities (J_c) of the superconducting films were measured by an inductive method. The correlation of optimum dopant concentration with microstructure, pinning and superconducting properties were scrutinized.

CHAPTER TWO
SUPERCONDUCTIVITY

2.1 Evaluation of Superconductivity

In 1911, H. Kamerlingh Onnes found that below 4.15 K of the DC resistance of mercury dropped to zero (Figure 2.1). The superconductivity was born with that finding. In 1912, Onnes discovered that the application of a sufficiently strong axial magnetic field restored the resistance to its normal value. In 1913, the element lead was found to be superconducting at 7.2 K. In 1930, the element niobium was found $T_c = 9.2$ K.
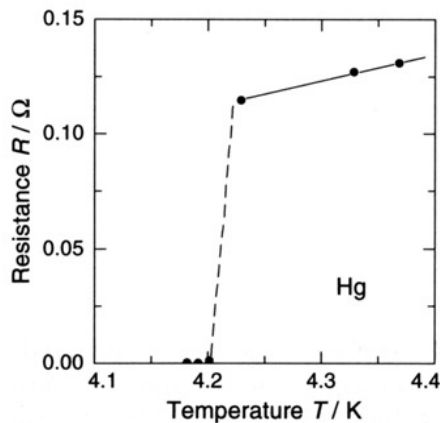
Figure 2.1 The resistance of mercury measured by Onnes (Owens & Poole, 1996)

In 1933, Meissner and Ochsenfeld found that when a sphere is cooled below its transition temperature in a magnetic field, it excludes the magnetic flux. In 1950, the theory of Ginzburg and Landau was published. This theory described superconductivity in terms of an order parameter and provided a derivation for the London equations. In the same year, H. Fröhlich predicted theoretically that the transition temperature would decrease as the average isotopic mass increased. This effect was called as the isotope effect and it was observed experimentally in the same year.

In 1957, the BCS microscopic theory was proposed by J. Bardeen, L. Cooper, and J. R. Schrieffer. In this theory, it is assumed that bound electron pairs that carry the

super current are formed and that an energy gap between the normal and superconductive states is created. The Ginzburg–Landau (1950) and London (1950) results fit well into the BCS formalism (Poole, Farach, Creswick & Prozorov, 2007).

In 1986, the highest known transition temperature was 23.2 K for a metallic compound made of niobium and germanium, with the chemical formula Nb_3Ge. The easiest way to observe the phenomenon, the compound is immersed in a cold liquid and cooled below its transition temperature. Before 1986 liquid helium (He) was usually used (Owens & Poole, 1996).

In the decade following the discovery of high-temperature superconductors (HTSs) in 1986, extensive international research led to the fabrication of HTS materials with a range of critical transition temperatures (T_c's) above the boiling point of liquid nitrogen, as well as to broad phenomenological understanding of their properties. These materials have been pursued for a variety of technologies, but the strongest driver has been the electric power utility sector. Electric power transmission through HTS power cables offers the chance to reclaim some of the power lost in the grid, while also increasing capacity by several times. Use of HTS conductors could also improve high-current devices, notably thanks to efficiency, capacity, and reliability. By the mid-1990s, despite many formidable technical problems, researchers had begun to realize viable first-generation HTS conductor technologies based on $Bi_2Sr_2Ca_2Cu_3O_{14}$ (BSCCO), which make available conductors that are suitable for engineering demonstration projects and for first-level applications in real power systems. Second-generation HTS conductors based on YBCO are currently poised to replace BSCCO, which will dramatically improve performance while also lowering costs (Sarrao et al., 2006).

Society has benefited tremendously from access to the refined, high-quality materials that enabled the computer revolution of the 20th century. The discovery two decades ago of superconductivity at remarkably high temperatures in the layered copper oxides has spurred many subsequent discoveries of novel exotic superconductors (Figure 2.2).
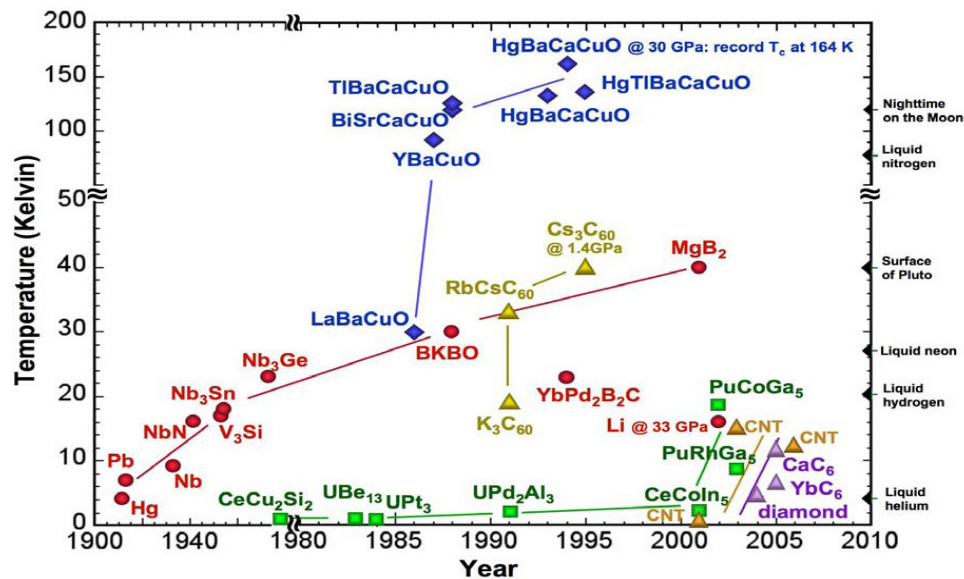
Figure 2.2 The observed superconducting transition temperature (T_c) of a variety of classes of superconductors is plotted as a function of time (Sarrao et al., 2006).

2.2 Theories of Superconductivity

2.2.1 Normal Conductivity

To understand the meaning of superconductivity and apprehend its unusual nature, it is required to comprehend normal conductivity (Owens & Poole, 1996). The electrical conductivity of a metal may be described most simply owing to the constituent atoms of the metal. The atoms lose their valence electrons, causing a background lattice of positive ions, called cations, to form, and the now delocalized conduction electrons move between these ions. The simplest approximation that we can adopt as a way of explaining conductivity is the Drude model. In this model it is assumed that the conduction electrons;

i.   Do not interact with the cations ("free electron approximation"),

ii.   Maintain thermal equilibrium through collisions, in accordance with Maxwell– Boltzmann statistics ("classical-statistics approximation"),

iii. Do not interact with each other ("independent-electron approximation").

Ordinarily, one abandons the free electron approximation by having the electrons move in a periodic potential arising from the background lattice of positive ions. An electron moving through the lattice interacts with the surrounding positive ions, which are oscillating about their equilibrium positions, and the charge distortions resulting from this interaction propagate along the lattice, causing distortions in the periodic potential. These distortions can affect the motion of yet another electron some distance away that is also interacting with the oscillating lattice. Propagating lattice vibrations are called phonons, so that this interaction is called the electron-phonon interaction (Poole et al. 2007).

Some electrons in the flowing current are scattered by defects and impurity in lattice. Because of these imperfections, normal metals have resistance. In the superconducting state, something must happen to electron waves so that they can move through the lattice without being scattered by its atoms (Owens & Poole, 1996).

In 1957 Bardeen, Cooper & Schrieffer published an article to explain the phenomenon of superconductivity. In 1972 these three researchers were awarded the Nobel Prize in physics for the theory in this paper, now commonly referred to as the BCS theory (Owens & Poole, 1996).

2.2.2 BCS Theory

BCS theory shows that for certain metals at low temperature, the presence of correlated bound pairs produces a state that is lower in energy than the normal state in which isolated electron waves move through the lattice in an uncorrelated fashion. It has a general law of nature that all physical systems seek to reach the lowest state of energy that they can attain. Thus BCS theory predicts the stability of a unique state in which probability waves of electron pairs move through a lattice without being scattered; this corresponds to a state of zero resistance. The formulation of BCS theory in terms of Cooper pairs held together by the lattice vibration mechanism

is known as phonon BCS; materials conforming to this formulation are known as conventional superconductors (Owens & Poole, 1996).

According to the BCS theory, as one negatively charged electron passes by positively charged ions in the conductor lattice, the lattice distorts. This in turn causes phonons to be emitted which form a trough of positive charges around the electron. Figure 2.3 illustrates a wave of lattice distortion due to attraction to a moving electron. Before the electron passes by and the lattice springs back to its normal position, a second electron is drawn into the trough. Then the two electrons which should repel one another, link up. The forces exerted by the phonons overcome the electrons natural repulsion. The electron pairs are coherent with one another as they pass through the conductor in unison. The electrons are screened by the phonons and are separated by some distance. When one of the electrons that make up a cooper pair and passes close to an ion in the crystal lattice, the attraction between the negative electron and the positive ion cause a vibration to pass from ion to ion until the other electron of the pair absorbs the vibration. The net effect is that the electron has emitted a phonon and the other electron has absorbed the phonon. Cooper Pairs keeps together with this exchange. It is important to understand that the pairs are constantly breaking and reforming. Since the electrons are indistinguishable particles, it is easier to think of them as permanently paired (Kayatekin, 2006).

The theory can also explain for other properties of the superconducting state, for instance the existence of a critical field. The critical field is the value of an applied magnetic field that supplies enough energy to separate electrons of Copper pairs. The interaction of tiny magnets of paired electrons with the applied field breaks up Copper pair. The superconducting gap and thus the binding energy of the pairs increase as the temperature is decreased below T_c; therefore the critical filed increases as temperature is decreased.

The origin of the quantization of the magnetic field inside the superconductor is also explained by BCS theory. In a Type II superconductor, there are thin thread-like filaments of normal conductivity called vortices. If the waves of all the electrons are

to be in phase at all times and at every point around the surface, the length of the waves must fit exactly around the circumference of the vortex to ensure that they connect smoothly; otherwise the phase relationship would be lost. In as much as the circumference must be an exact multiple of the wavelength for this to happen, it follows that only certain wavelengths are allowed and thus only certain energies. Since the energy of the electrons is quantized, so is the magnetic field produced by their motion (Owens & Poole, 1996).
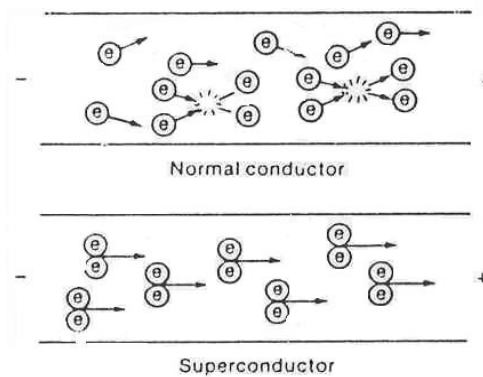
Figure 2.3 Schematic illustrating the difference, according to the BCS theory, between normal conduction and zero-resistance superconduction (Owens & Poole, 1996).

2.2.3 Meissner Effect

The second characteristic property of the superconducting state was discovered by Alexander Meissner and R. Ochsenfeld. This phenomenon is called Meissner effect. They discovered that when a superconducting metal is placed in a magnetic field and then cooled below the transition temperature, the magnetic field is expelled. According to their discovery, when a metal is in the superconducting field no magnetic field is allowed inside it. Figure 2.4 illustrates how an ideal conductor and a superconductor behave under magnetic field.
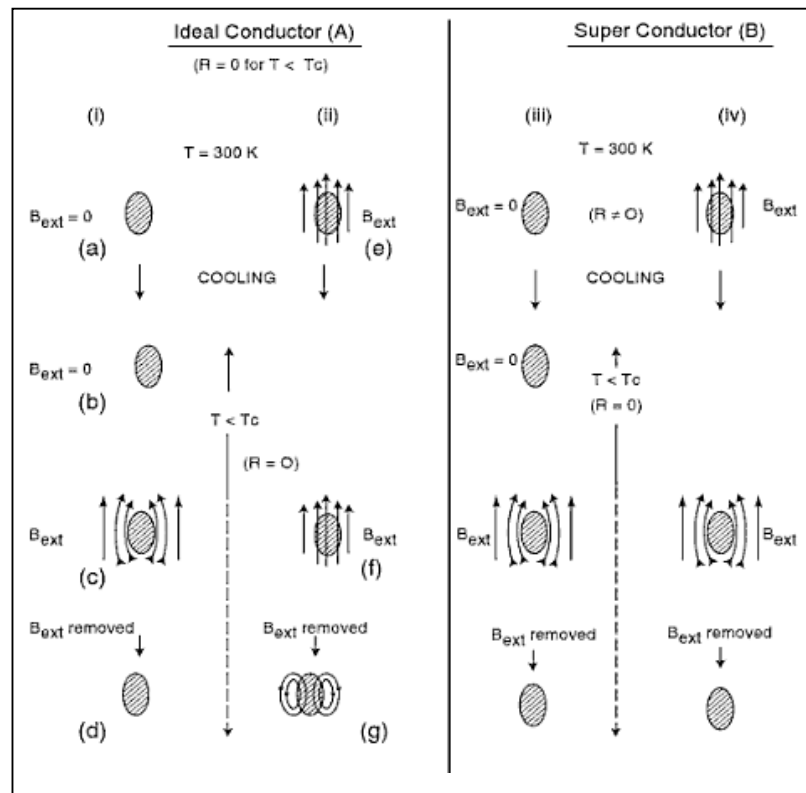
Figure 2.4 Comparison of magnetic behaviors of an ideal conductor and a superconductor. Both have R=0 for T<Tc (Saxena, 2010).

On switching off B_{ext} in the cooled state, this requirement is satisfied (in both A and B section of Figure 2.4), because the process of switching off B_{ext} induces persistent currents inside the material surface, which maintain the value of magnetic field in the interior. In ideal conductor may adopt two different states (Figure 2.4.c) or (Figure 2.4.f) depending on the order of events leading to this state. Thus, we have two different states (Figure 2.4.d) and (Figure 2.4.g) for an ideal conductor. However, if a superconductor was merely such an "ideal conductor", the superconducting state would not be a state in the thermodynamic sense. The Meissner effect, which represents the property of ideal diamagnetism, follows independent of vanishing of electrical resistance. However, if cooling is done after the application of external field, an ideal conductor does not show ideal diamagnetism, for example external field is not expelled (Saxena, 2010).

A more detailed analysis of this situation shows that some magnetic field does indeed penetrate surface layers of the superconductor, and it is present where the surface current flows. The statement that the superconductor has no magnetic field inside refers to the bulk of material, not to surface regions. The surface layer where penetration occurs has a thickness called the London penetration depth, denoted by the symbol λ_L. The value of the penetration depth λ_L is a characteristic of each individual superconducting material; typical values range from 0.2-0.8 µm. The penetration depth increases with increasing temperature as the transition temperature is approached below.

The Meissner effect can be measured using both DC and AC magnetic fields. For DC measurement, the magnetometer is placed close to the surface of the sample located in a magnetic field. As the sample cooled below its T_c, the field inside of sample expelled and the resulting increase in the magnetic field strength outside the surface of the superconductor is detected by the magnetometer. The operation of a very sensitive superconducting quantum interference devices (SQUID) magnetometer depends on its superconducting properties. This device is employed for this measurement.

Using AC method, two small coils are wound around the superconducting sample, an inner exciting coil and an outer probe coil; the latter is attached to a voltmeter. When an AC voltage is applied to the exciting coil, the resulting current flow causes an AC magnetic field to sweep across the sample. This causes an AC voltage in the probe coil that is detected by the voltmeter. When the sample cooled below T_c, the AC magnetic field is excluded from it, causing the AC field outside the sample to increase and thereby increase the voltage induced in the probe coil. The increase in probe voltage is proportional to the strength of the magnetic field ejected from the sample; therefore it measures the magnitude of the Meissner effect (Owens & Poole, 1996).

2.2.4 London Equation

The Meissner effect could not be explained by any conventional model of electricity in solids, but a bold hypothesis was put forth by F. and H. London: Since current flows unimpeded within a superconductor, let there be circulating currents inside the superconductor which set up a magnetic field that exactly cancels the magnetic field being applied externally. The form required for such a circulating current turns out to be surprisingly simple.

Recalling that magnetic field B is related to the vector potential **A** by B= ∇x**A**, the London hypothesis makes the current density j linearly proportional to **A**:

$$j = \frac{-1}{\mu_o . \lambda_L^{~2}} . A \qquad\qquad (2.1)$$

This so-called London equation is dramatically different from the normal Ohm's law, j = σ.E. From here on, Maxwell's equations do the rest. The vector potential can be exchanged for the magnetic field by taking the curl of both sides and obtaining,

$$\nabla . j = \frac{-1}{\mu_o . \lambda_L^{~2}} . B \qquad\qquad (2.2)$$

But we know from Maxwell's equations that, in the absence of a time-varying electric field,

$$\nabla . B = \mu_0 . j \qquad\qquad (2.3)$$

taking the curl of this equation, we have

$$\nabla . \nabla . B = \mu_0 . \nabla . j \qquad\qquad (2.4)$$

Now, another Maxwell equation says $\nabla . B = 0$, so this reduces to

$$-\nabla^2 . B = \mu_0 . \nabla . j \tag{2.5}$$

and invoking Equation (2.2) above, this yields,

$$\nabla^2 . B = \frac{1}{\lambda_L^2} . B \tag{2.6}$$

The only constant solution inside the superconductor must be B = 0, which is another way of saying that magnetic fields are excluded. The variable solution has the general form

$$B(x) = B_0 . \exp(-x / \lambda_L) \tag{2.7}$$

This explains the contrivance of the proportionality constant relating j to **A**. The value λ_L is called the *London penetration depth.*

The hypothesis of circulating shielding currents thus gives a concise account of the Meissner effect; j ∞ **A** is all that is needed. Years later, when the BCS theory came along and justified the London equation, the issue was settled satisfactorily (Sheahen, 2002).

2.2.5 The Ginzburg-Landau Theory

In 1950, Ginzburg and Landau proposed a theory based on Landau's general theory of 2nd order phase transitions. The superconducting electrons were described by a complex wave function, ψ, such that $ns = |\psi|2$. By expanding the expression for the free energy, a differential equation may be derived for ψ:

$$\frac{1}{2m}(-i\nabla + 2e.A)^2 \Psi + (\alpha + \beta \Psi \Psi *)\Psi = 0 \tag{2.8}$$

The super current density is given by:

$$J_s = \frac{ie}{m}.(\Psi * \nabla\Psi - \Psi\nabla\Psi *) - \frac{4e^2}{m}A\Psi\Psi * \qquad (2.9)$$

where **A** is the magnetic vector potential such that B = curl **A**.

The Ginzburg-Landau equations lead to two characteristic lengths, the G-L penetration depth, λ_{GL},

$$\lambda_{GL} = \sqrt{m\beta / 4\mu_0 e^2 |\alpha|} \qquad (2.10)$$

and the coherence length, ξ

$$\xi = \sqrt{\hbar^2 / 2m|\alpha|} \qquad (2.11)$$

in which α is proportional to (T-T$_c$) and β is approximately independent of T.

The penetration depth is, like the London penetration depth, the characteristic length for the decay of the magnetic field in a superconductor. The coherence length may be described as the length scale over which the order parameter varies. As both λ_{GL} and ξ are inversely related to α, they are dependent on temperature and both diverge as T approaches T$_c$. However, the ratio of the parameters,

$$K = \lambda_{GL} / \xi \qquad (2.12)$$

This is known as the Ginzburg-Landau parameter, independent of α and because of this it is approximately independent of temperature (Birlik, 2011).

2.2.6 Levitation

A specially fascinating and compelling manifestation of the Meissner effect is called levitation. A superconductor expels a magnetic field causes it to be repelled by

a magnetic field in its vicinity and to move away from nearby magnetic fields. A magnet is an object that produces magnetic field around it, so it is natural to expect a superconductor and a magnet to repel each other. This reciprocal recoil is responsible for the phenomenon of levitation. A thin slab of the superconductor is cooled below its transition temperature by placing it in a pool of liquid nitrogen, and then a magnet with dimensions smaller than those of the slab is placed above the slab. The reciprocal recoil between the slab and the magnet induces the magnet to be levitated, held suspended in space above the superconductor (Owens & Poole, 1996).

2.2.7 Critical Magnetic Field and Critical Current Density

There is an upper limit to the strength of the magnetic field B_{app} that can be applied to a superconductor without destroying its superconducting properties. If a metal is in the superconducting state and B_{app} is slowly increased, the field eventually reaches a value that removes the material from the superconducting state. The magnitude of the magnetic field that does this is called the critical field B_c. The value of B_c depends on material. For a special superconductor, the magnitude of this critical field B_c (T) increases as the temperature is decreased below the T_c. Figure 2.5 shows this temperature dependence for a superconductor (Owens & Poole, 1996).
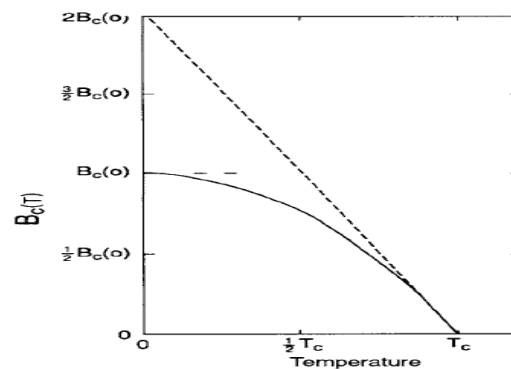
Figure 2.5 Temperature dependence of the critical field B_c(T) (Poole, 1999).

There is a maximum amount of current that can flow before superconducting state is removed. This is called critical current density J_c. This is a direct consequence of the existence of the critical magnetic field, because the current produces a magnetic

field and a magnetic field produces a current. A critical current produce a magnetic field at the surface of the material that quenches the superconducting state (Owens & Poole, 1996).

The critical field B_c and critical current J_c are related to each other through the simple expression:

$$B_c = \mu_0 . \lambda_L . J_c \tag{2.13}$$

where μ_0, called the permeability of free space, is a universal physical constant with the value;

$$\mu_0 = (4.\pi).10^{-7}.N/A^2 \tag{2.14}$$

where N is the unit force. We use tesla for B_{c2}, meter for λ_L and ampere per square meter for J_c. J_c (T) has temperature dependence similar to that of the critical field, as indicated by the J_c (T) curve in Figure 2.6.
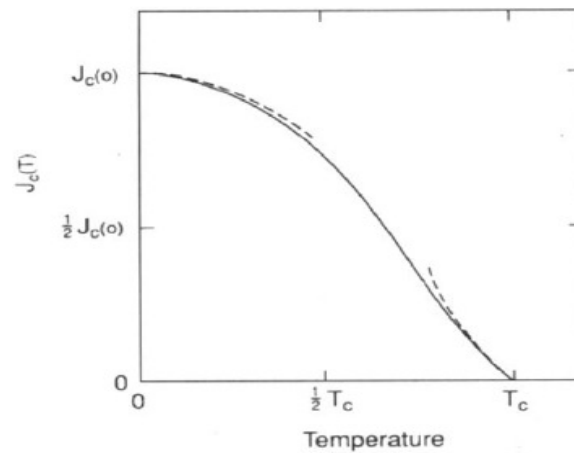
Figure 2.6 Temperature dependence of the critical current density J_c (T) (Poole, 1999).
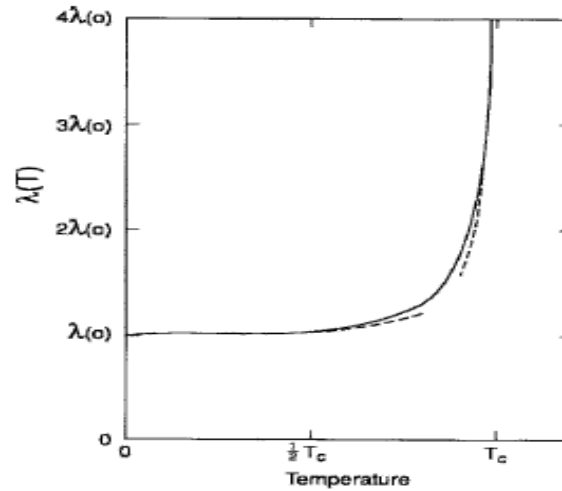
Figure 2.7 Temperature dependence of the penetration depth λ_L (T) (Poole, 1999).

The penetration depth λ_L (T) also depends on the temperature; its smallest value is at absolute zero and it becomes very large as the critical temperature is approached. As mentioned before the penetration depth increases with increasing temperature as the transition temperature is approached from below. Figure 2.7 shows temperature dependence of the penetration depth λ_L (T).

2.2.8 Type I and Type II Superconductors

There are two types of superconductor including type I and type II. Because of the impressive difference in their magnetic and current-carrying properties, they are also known as *soft* and *hard* superconductors. Whilst overall industry is based on type II superconductors, type I superconductors have only very limited applications.

Superconductors have a critical temperature (T_c), a critical magnetic field (H_c) and a critical current density (J_c) as well. That there must be some upper limit to the current density in a superconductor is required by the relationship between current and magnetic field; for a wire of radius *a* carrying current *I*, the magnetic field at the surface is (I/2πa). The current cannot exceed the amount that produces a critical magnetic field (H_c) at the superconductor, which implies a critical current $I_c = 2\pi a H_c$,

and $J_c = 2H_c/a$. For real superconductors, the real J_c is less than this upper limit and the actual current is limited by other physical mechanisms.

For a type I superconductor, critical current is simply a consequence of critical magnetic field. Since H_c is low in type I superconductors, their critical current densities are likewise low. Because of this type I superconductors have not been of interest to the electric utilities or magnet builders.

In a type II superconductor, the relationship is much more complicated; indeed, Figure 2.8 shows the critical surface in the 3D space of temperature, magnetic field, and current. This is known as a THJ plot, after the three axes. The critical current is no longer related in a trivial way to the magnetic field.

The response to an applied magnetic field is quite different in the two cases. The behavior of a type I superconductor: there is exact cancellation of an applied magnetic field H by an equal and opposite magnetization M, resulting in B = 0 inside the superconductor. Superconductivity disappears above the critical field,.

In type II superconductors, the Meissner effect is partially blocked. At a lower critical field (H_{c1}) the magnetic field starts penetrating into the material. Penetration increases until at the upper critical field (H_{c2}) the material is fully penetrated and the normal state is restored. This behavior is shown in Figure 2.9, in which magnetization increases to a negative maximum but then it retreats as flux lines begin to penetrate. The cancellation of magnetic field by magnetization is no longer perfect, and B is finite within the superconducting material. Therefore we seem to have a major breach of the principle that superconductors exclude magnetic fields, for obviously magnetism and superconductivity co-exist in a type II material (Sheahen, 2002).
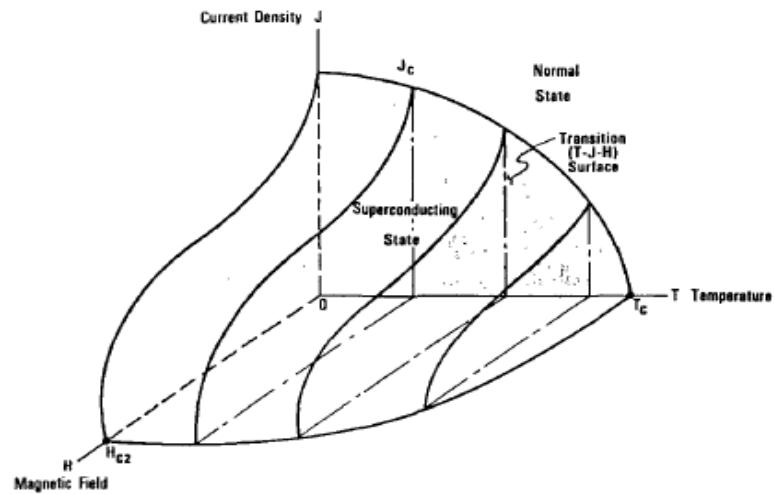
Figure 2.8 The relationship between temperature, magnetic field and critical current in a superconductor (Sheahen, 2002).
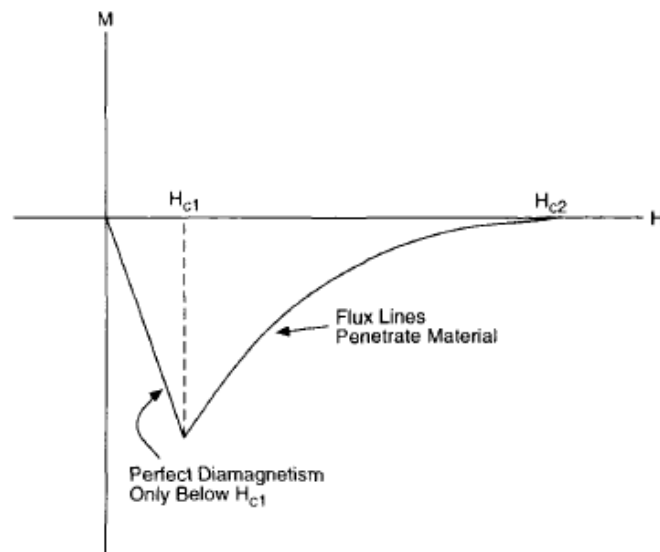
Figure 2.9 Magnetization as a function of applied magnetic field for an ideal type II superconductor (Sheahen, 2002).

2.3 Superconducting Materials

2.3.1 Low Temperature Superconductors

Elements in a particular column of periodic table have the same number of valance electrons (Ne). The alkali elements of lithium (Li), sodium (Na),

potassium (K), and cesium (Cs) have high conductivity and they all in the first column, Ne=1. Some elements in the periodic table as Li, Ba, Cr, Pd, Se, Sb, Te, Bi, Ce and Eu cannot be made superconductive by simple cooling them. They become superconductor only when irradiated, subjected to high pressure or made into thin films. The great majority of the superconducting elements are Type I. These elements have low T_c and B_c, so they are not convenient for applications. Generally speaking T_c of some elements is raised dramatically by preparing them in thin films for instance; the T_c of tungsten (W) was raised from its bulk value of 0.015 K to 5.5 K in a film.

Among the elements, niobium not only has the highest T_c, but it is also a component of many higher T_c compounds, like Nb_3Ge. T_c of binary alloys can be higher than that of both elements, between the two values or lower than either one alone (Owens & Poole, 1996). The highest T_c of the older superconductors were obtained with the A-15 compounds A_3B. A notation is used for elements and B for AB compounds. Typical A-15 compounds A_3B only form for the 3:1 ratio of A atoms to B atoms. This ratio is important to produce higher T_c. Even though A-15 compounds exhibit the highest T_c of the classic superconductors, they are not widely used in applications because they are too brittle and not flexible enough to be drawn into wires.

There are a number of superconducting binary compounds AB in which A is a metallic element and B is a nonmetallic element. Examples are NbN (T_c= 17 K) and MoC (T_c= 14.3 K). In addition to these, there are several dozen metallic AB_2 compounds called Laves phases that are superconducting. Some of them have $T_c$ above 10 K and high B_c. These materials also have the advantage of not being so hard and brittle as some other compounds and alloys with comparable T_c.

The Chevrel-phase compounds $A_xMo_6X_8$ are mostly ternary transition metal compounds, where A can be almost any element and the element X is one of the S, Se or Te. These compounds have relatively high T_c and critical magnetic fields B_{c2} of several Tesla, but their critical currents are favorably low (Owens & Poole, 1996).

2.3.2 High Temperature Superconductors

There would be a lot more practical uses for superconductivity if it were not for the very high cost of liquid helium coolant. Any gas will liquefy at sufficiently low temperatures; for instance, oxygen becomes liquid at 90 K and nitrogen at 77 K. It is far less costly to liquefy these gases than to liquefy helium. For any application in which liquid nitrogen can replace liquid helium, the refrigeration cost will be about 1000 times less.

There are several ceramics, based on copper oxide, which remain superconducting near 100 K. For example, T_c of YBCO has been found 92 K. Additional important ceramic superconductors include bismuth strontium calcium copper oxide (BSCCO) thallium barium calcium copper oxide (TBCCO) and mercury barium calcium copper oxide (HBCCO). Table 2.1 presents the chemical formulas and T_c values for each of these compounds.

Table 2.1 High Temperature Superconductor Materials (Sheahen, 2002).

Name	Formula	Transition Temperature (K)
Yttrium barium copper oxide	$YBa_2Cu_3O_7$	92
Bismuth strontium calcium copper oxide	$(BiPb)_2Sr_2Ca_2Cu_3O_x$	105
Thallium barium calcium copper oxide	$TlBa_2Ca_2Cu_3O_y$	115
Mercury barium calcium copper oxide	$HgBa_2Ca_2Cu_3O_y$	135

The ceramic superconductors of greatest interest are very anisotropic compounds; that is, their properties are quite different in different crystalline directions. Because of this, researchers take considerable exertions to obtain good grain alignment within any finite-sized sample. The structure is essentially that of a sandwich, with planes of copper oxide in the center, and that is where the superconducting current flows. The compounds BSCCO and TBCCO are even more evident in their anisotropy; in fact, very little current can flow perpendicular to the copper oxide planes in those lattices.

The role of the elements other than copper and oxygen is secondary. In YBCO, yttrium is only a spacer and a contributor of charge carriers; indeed, nearly any of the

rare earth elements (holmium, erbium, dysprosium, etc.) can be substituted for yttrium without changing the T_c significantly. Often the formula is written as $(RE)_1Ba_2Cu_3O_7$, to emphasize the interchangeability of other rare earths (RE) with yttrium.

The bismuth compounds show the interesting property of being *micaceous*; that is, they are like mica. The crystal lattice shears easily along the bismuth oxide planes and this allows BSCCO to be deformed and shaped with less difficulty than the other ceramic superconductors. This advantage has led researchers to invest more effort in making wire out of BSCCO: lengths of over one kilometer have been made so far.

Unfortunately, the new high-temperature superconductors have two major disadvantages: they are very brittle and they do not carry enough current to be very useful. The idea of making wire out of ceramics would be a subject of decision, were it not for the example set by fiber optics. It is true that if one makes a strand of sufficiently tiny diameter, then a cable made from such strands can have a bending radius of a few centimeters without over-straining the individual strands. For the high temperature superconducting materials, the engineering task of overcoming brittleness is proving more difficult than it was for fiber optics.

A more important disadvantage is that the magnetic properties of these materials are substantially different from conventional metallic superconductors. The workhorse material of low temperature superconducting magnets, niobium-titanium (NbTi), allows lines of magnetic flux to penetrate in such a way that these lines tend to stay put: the phenomenon is known as flux pinning. By contrast, the exceptional crystalline structure of the copper oxide superconductors causes the magnetic flux lines to fragment, and hence they move around readily, thus dissipating energy and defeating the advantage of superconductivity. In one of those perverse conspiracies of nature, the crystal line properties that offer the best chance to circumvent the brittleness problem are the very same properties that tend to degrade flux pinning (Sheahen, 2002).

2.3.2.1 Properties of YBCO

YBCO is one of the most widely studied high temperature superconductor, because of its promising and attractive aspects of applications, which include energy storage systems, current limiters, magnetic bearings, etc., above liquid nitrogen temperature (77K) (Jha & Khare, 2010).

YBCO has an orthorhombic crystal structure consisting of three perovskite-like unit cells stacked along the c-axis (the perovskite structure has the general formula ABO_3). The lattice parameters are: $a=3.82$Å, $b=3.88$Å and $c=11.67$Å. YBCO exists in either a tetragonal or an orthorhombic crystal structure (see Figure 2.10), being only superconducting in the orthorhombic phase. The central cell has a Y atom situated between two CuO_2 planes.
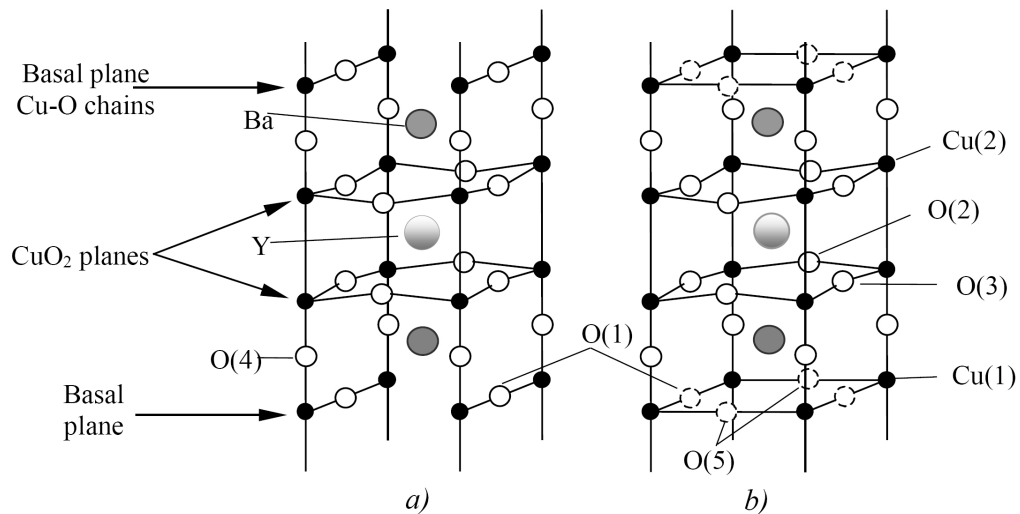
Figure 2.10 Crystal structures of (a) orthorhombic YBCO and (b) tetragonal YBCO. As it can be seen, O (5) position is not occupied in (a) (Apetrii, 2009).

Above and below these CuO_2 planes is a BaO_2 layer, on top of which a Cu-O basal plane with variable oxygen content is present (Figure 2.10). In the orthorhombic phase the oxygen sites are ordered into Cu-O chains along the b-axis, while in the tetragonal phase the oxygen sites in the basal plane are equally occupied. In the orthorhombic phase, superconductivity occurs in the CuO_2 planes. The CuO_2 planes contain mobile charge carriers (holes) and the Cu-O chains act as a charge reservoir that transfer holes to the planes. The oxygen content in YBCO determines

its crystallographic structure (Figure 2.11.a) and the hole concentration in the CuO_2 plane. In Figure 2.11.a, TN represents the Néel temperature of the antiferromagnetic phase, and T_c the critical temperature of the superconducting phase.

For an oxygen content $x = 6$, the compound $YBa_2Cu_3O_6$ is in the tetragonal phase and an insulator (antiferromagnetic state). Increasing the oxygen content up to $x = 6.6$ the compound experiences a phase transition from tetragonal to orthorhombic (metallic state). From Figure 2.11.b, it can be seen that by raising the oxygen content up to 6.94, T_c approaches its maximum value (93 K). Above $x = 6.94$, T_c drops by about 4 K. The maximum T_c value found for $x = 6.94$ is due to an optimum hole doping of the CuO_2 planes. The drop in T_c for x above 6.94 can be explained as an over doping, where the holes in the CuO_2 planes exceed the optimum concentration (Apetrii, 2009).
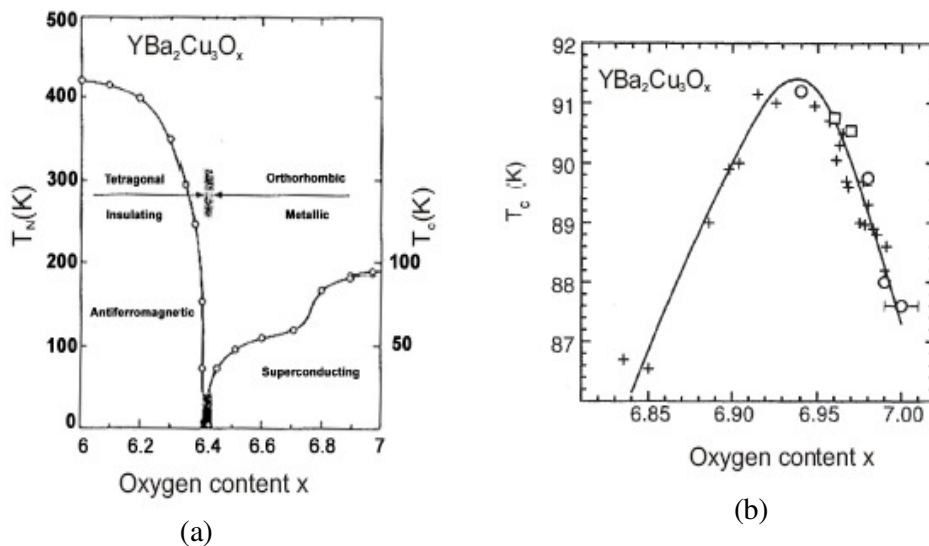
Figure 2.11 (a) Phase diagram of the $YBa_2Cu_3O_x$ system as function of the oxygen content and (b) Variation of T_c with oxygen content (Apetrii, 2009).

2.4 Flux Vortices, Pinning and Critical Currents in Type II Superconductors

Vortex matter is an ensemble of discrete magnetic flux tubes. Each vortex is created by superconducting electrons circulating around a non-superconducting "normal" core. These Abrikosov vortices appear in a superconductor in the presence

of an external magnetic field above a certain field limit. In pure superconductors, these vortices form a triangular array similar to a crystalline solid. Like solids, these ordered arrays of vortices can melt at high temperatures, leading to a liquid of wriggling magnetic field lines. Great strides have been made in vortex physics since the discovery of high-temperature superconductors in the cuprates because vortices are present in these materials over a much wider range of temperature and magnetic field than in the low-temperature superconductors previously available.

A superconducting vortex can be viewed as a magnetic micro-tornado, as shown in Figure 2.12.a. The eye of the tornado corresponds to the normal vortex core, which is surrounded by encircling super currents. Two lengths characterize the vortex: The London penetration depth, λ_L, measures the radial extent of the circulating currents, and the coherence length, ξ, is roughly the size of the normal-conducting core.

When two parallel vortices come close to each other, they repel one another, as shown in Figure 2.12.b. As a result of the circulating currents, the vortices can be viewed as small solenoid magnets, each with its north pole on the top and its south pole on the bottom. Thus, they will repel each other just like two parallel bar magnets. This mutual repulsion enforces vortices to arrange themselves as far apart as possible within the confines of the superconducting sample. The resulting vortex arrangement is a periodic structure called the Abrikosov vortex lattice. This lattice usually has a hexagonal pattern.

Sending an external current through a superconductor in the presence of a magnetic field induces a so-called Lorentz force, F_L, on the vortices, where $F_L = \Phi_0 J$, with Φ_0 being the magnetic flux quantum carried by each vortex and J being the applied current density (Figure 2.13.a). When superconductors contain non-superconducting normal inclusions due to structural defects, vortices will place themselves on these "defected" sites, thereby minimizing their superconducting energy. This phenomenon, called vortex pinning, forms the foundation for all electro-technical applications of superconductors (Figures 2.13.a and 2.13.b). The vortices experience an attractive force, F_p, which pins them to these defected sites.

When the applied current is large enough that is $F_L > F_P$, the vortices become dislodged from the pinning sites and move. A moving vortex induces a resistance as the normal core of the vortex is dragged through the superconducting matrix. The applied current density at which $F_L = F_p$ is the critical current density, J_c. Generally, J_c decreases with increasing temperature and magnetic field and reaches zero at the so-called "irreversibility line," $H_{irr}(T)$. Above this line, the superconductor does not carry loss-free current.
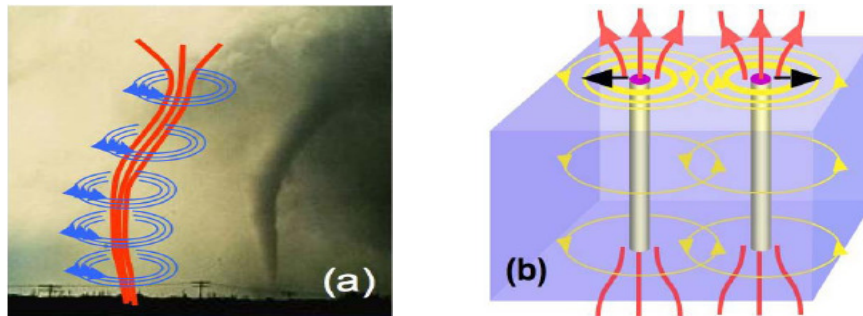
Figure 2.12 (a) A tornado and (b) schematic view of vortex (Sarrao et al., 2006)

High-temperature superconductors contain a high concentration of natural pinning sites, such as oxygen vacancies. To improve the electrical properties of superconductors, one can also manufacture pinning centers artificially, optimizing their shape, size, and arrangement. Linear defects, such as columnar defects produced by irradiation of superconductors with high-energy heavy ions (e.g., Au, Pb, and U) and dislocations, have proven to be among the most efficient pinning centers. The linear and planar correlated defects are found in YBCO conductors. On account of their geometric match to the vortices, these correlated defects are more effective in pinning the vortices than are randomly placed point defects, which, as shown in Figure 2.13.b, require a vortex line to contort - at the cost of elastic energy - in order to accommodate the pinning sites. Pinning centers with diameters on the order of the coherence length ξ (the size of the normal vortex core) are optimal for pinning individual vortices: Smaller sites cannot fully accommodate the vortex core (and therefore, some energy has to be spent suppressing superconductivity to create the core), while bigger sites waste too much of the useful superconducting body. Nonetheless, large sites can pin several vortices simultaneously. The problem of

artificially creating pinning sites matched to each superconducting material's specific vortex core size and optimizing their performance for application specific temperature and field operating conditions is a challenge that is being tackled through recent advances in nanotechnology.

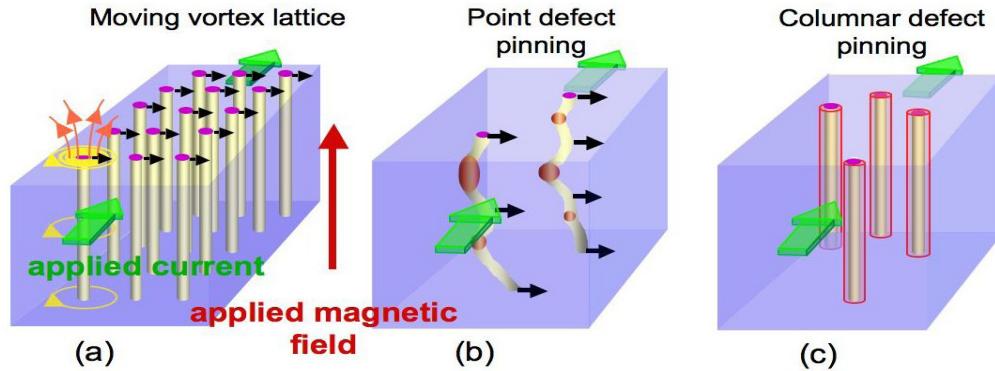Figure 2.13 (a) Schematic of vortices moving under a Lorentz force (black arrows) induced by an applied current (green arrow) and a magnetic field (red arrow) in a clean sample free of defects. (b) Sections of vortices pinned by point defects (oxygen vacancies, precipitates, or defects induced by electron irradiation). (c) Entire sections of vortices are pinned by line defects, such as amorphous columnar tracks induced by high-energy heavy ion irradiation (Sarrao et al., 2006).

The large thermal energies that are necessary corollaries of the fact that superconductivity in cuprates exists at relatively high temperature add another challenge to the vortex-pinning scenario. Namely, at relevant temperatures, even when the applied current is subcritical ($J < J_c$), the thermal energy can promote vortex jumps between neighboring pinning sites, resulting in a finite resistance even at low currents (Figure 2.14.a). This vortex creep phenomenon is due to the random distribution of the pinning centers. In this situation, the vortices adjust themselves to the disorder. Each vortex bends, trying to find the energetically best position (ground state) among the pinning sites (Figures 2.13.b and 2.14.b). Thanks to the random distribution of the pinning centers, these positions are not unique, and different vortex configurations with equal energies are possible. This phenomenon is called degeneracy of the low-lying energy states, and it is the main characteristic of the glassy state. Due to the randomness, this degeneracy exists on every spatial scale. The degeneracy results in the complex hierarchical nature of the energy relief of all glasses and gives rise to the peculiar glassy dynamics of creep. Vortex creep is

highly nonlinear and non-Ohmic and can manifest itself in aging and memory effects. It sets the fundamental lower achievable limit for power losses due to vortex motion (Figure 2.14). Vortex creep and the slow decay of critical currents are serious concerns, especially for potential applications requiring highly stable magnetic fields, as in magnetic resonance imaging (MRI) magnets. Finding effective ways of suppressing the strong flux creep that is responsible for the reduced irreversibility field H_{irr} of high-T_c superconductors is one of the major challenges for vortex matter science (Sarrao et al., 2006).
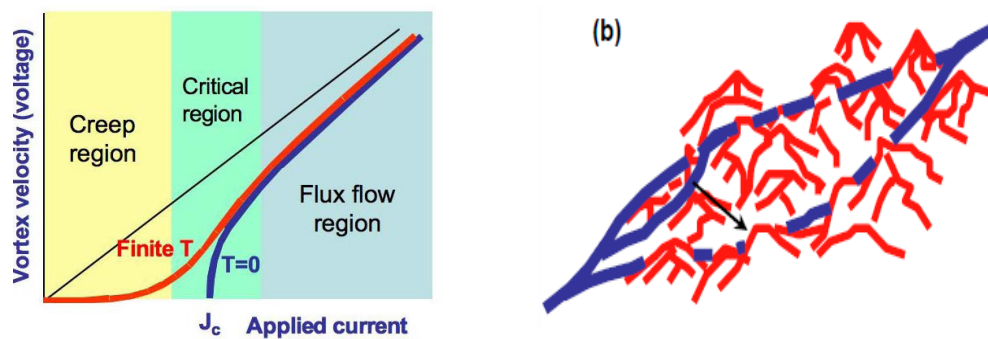
Figure 2.14 (a) Vortex dynamics in the glassy state. Because of vortex creep, there is finite resistance even at currents well below J_c (red curve) at finite temperature, in contrast to $T = 0$ (blue line). (b) Illustration of a single vortex (blue) residing on top of a pinning energy landscape, which can be visualized as mountains and valleys (red). In the vortex creep process, the vortex can hop (black arrow) from one valley to another as a result of thermal fluctuations (Sarrao et al., 2006).

2.5 Applications of Superconductors

The major commercial applications of superconductivity in the medical diagnostic, science and industrial processing fields listed below all involve low temperature superconductor (LTS) materials and relatively high field magnets. Indeed, without superconducting technology most of these applications would not be viable.

• Magnetic Resonance Imaging (MRI),
• Nuclear Magnetic Resonance (NMR),
• High-energy physics accelerators,
• Plasma fusion reactors,

• Industrial magnetic separation of kaolin clay.

Several smaller applications utilizing LTS materials have also been commercialized, e.g. research magnets and Magneto-Encephalography (MEG). The latter is based on Superconducting Quantum Interference Device (SQUID) technology which detects and measures the weak magnetic fields generated by the brain. The only substantive commercial products incorporating HTS materials are electronic filters used in wireless base stations. About 10,000 units have been installed in wireless networks worldwide to date.

Superconductor-based products are extremely environmentally friendly compared to their conventional counterparts. They generate no greenhouse gases and are cooled by non-flammable liquid nitrogen (nitrogen comprises 80% of our atmosphere) as opposed to conventional oil coolants that are both flammable and toxic. They are also typically at least 50% smaller and lighter than equivalent conventional units which translate into economic incentives (Overview of application, 2012).

CHAPTER THREE

CHEMICAL SOLUTION DEPOSITION PROCESS

There are many processes for making YBCO superconductor films. Typical ones are pulsed laser deposition (PLD), thermal evaporation, metalorganic chemical vapor deposition, liquid phase epitaxy, *ex situ* electron beam processing, metalorganic deposition (MOD) and the sol-gel process. Among them, PLD is predominant for fabricating YBCO films and it has produced YBCO films with a relatively high J_c. On the other hand PLD has two major problems: it requires an expensive vacuum system and the high-power UV laser. This UV laser is also very expensive to run (Araki & Hirabayashi, 2003). Chemical solution deposition (CSD) is substantially considered the most promising route to the low-cost commercial production of HTS wires due to its advantages, including inexpensive non-vacuum equipment, precise control of metal–oxide precursor stoichiometry, ease of compositional modification on a molecular level, high deposition rates on large areas, and potentially near 100% utilization of the precursor material. Furthermore, deposition techniques such as dip coating, spray coating, and printing methods allow scalability. CSD processes have proven to be a viable low-cost high-volume manufacturing technology for high-performance long-length practical wires competitive with established physical deposition methods (Knoth et al., 2007).

3.1 Chemical Solution Deposition (CSD)

Solution chemistry is becoming a very promising path toward low-cost preparation of functional thin-film materials and nanostructures. Many different types of functional oxides (ferromagnetic, superconducting, ferroelectric, etc.) have been prepared, displaying performances that are competitive with physical deposition methodologies where high vacuum equipment is required.

A key goal for solution-based techniques is to achieve a detailed understanding and control of the four steps involved in the process, together with their mutual interrelationship:

i. Precursor chemistry and solution preparation,

ii. Solution deposition,

iii. Decomposition of the chemical precursors toward an intermediate amorphous and/or nano crystalline solid,

iv. Nucleation and growth of the final crystalline materials.

Previous studies demonstrated that a complex relationship exists among the processing parameters, microstructure, and performances. Therefore, a thorough investigation of the mechanisms involved in the microstructural evolution at different steps is required, together with knowledge of its influence on the final performances of the functional materials. Coated conductors (CCs), which are based on YBCO, are a second generation of high-current conductors that display outstanding performance at temperatures and magnetic fields much higher than any other known superconducting material. Therefore, they have opened a new avenue for the applications of superconductivity in power systems and magnets. However, to achieve the required performance, an unavoidable hurdle is to develop high-throughput methodologies which, additionally, must be efficient to produce the long-length highly textured multilayered architecture required for such CCs. CSD has been demonstrated to be a very promising technique for the large-scale production of CCs (Obradors et al., 2009).

The manufacture of thin films using this process involves four basic steps (Figure 3.1);

i. Preparation of the precursor solution,

ii. Deposition of the film onto the substrate,

iii. Low-temperature heat treatment for drying and pyrolysis of the organic compounds (up to $600^{o}C$),

iv. Higher temperature heat treatment for the crystallization of the film into the desired oxide phase ($600^{o}C$- $1200^{o}C$).
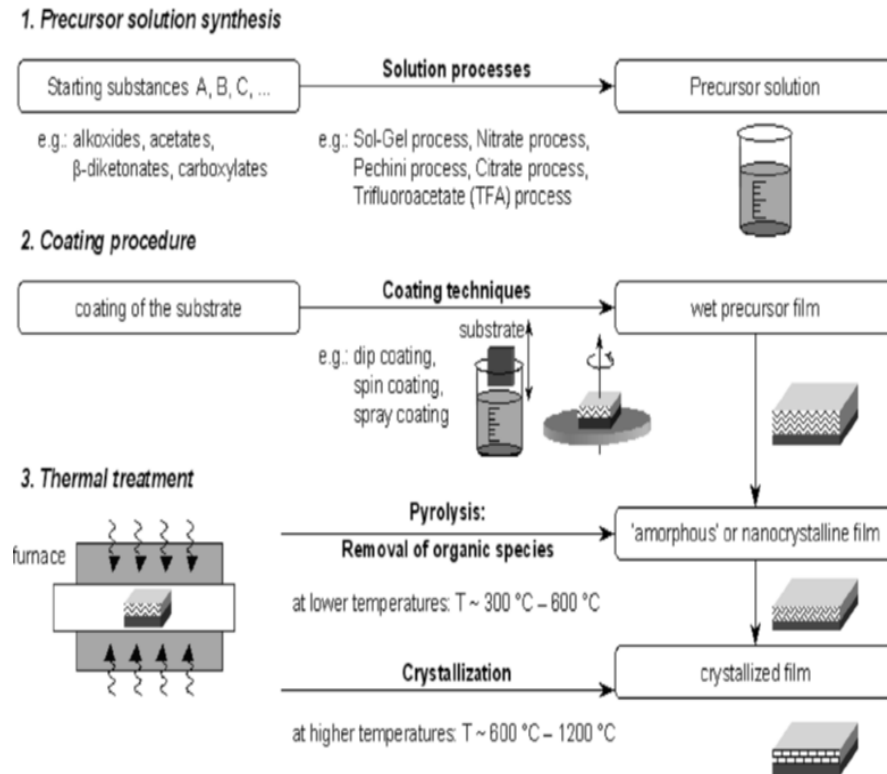
Figure 3.1 Overview of the chemical solution deposition process (Knoth et al., 2006).

The last three steps are similar for most solution deposition processes. They have differences in the characteristic of the precursor solution. The substrates and the processing conditions for using the CSD technique, some requirements must be executed by the solution chemistry;

   i. Sufficient solubility of the precursor salts in the solvent to obtain a stable solution,

  ii. No macroscopic phase separation of precursor components during drying or pyrolysis,

 iii. Acceptable wetting of the substrate,

 iv. Solution rheology adjusted to the deposition approach and deposition parameters to avoid thickness variation,

  v. Sufficient long-term stability of the solution to avoid non-reproducible film properties.

Chemical solution deposition has some advantages over conventional methods. The first advantage is the precise control of the composition. Secondly this method gives a wide flexibility in the substrate choice and, finally, the most important advantage is the lower cost of this method for coating large areas since vacuum technology is not required. Further advantages of this process are the simplicity of different precursor solutions preparation and the fact that it is a process which can be modified in order to synthesize a new material system (Apetrii, 2009).

The wide range of chemical routes available for the synthesis of appropriate precursor solutions can be divided mainly into classical sol–gel processes and metal organic decomposition (MOD) processes. Sol–gel processes commonly start from metal alkoxides undergoing hydrolysis and condensation reactions, leading to a colloidal solution, called sol, and finally to the formation of a three-dimensional gel network. MOD processes are based on metalorganic educts insensitive to hydrolysis, such as carboxylates (e.g. acetates, ethyl hexanoates) or b-diketonates (e.g. pentanedionates), that are decomposed during pyrolysis after evaporating the solvents of the as-deposited layer (physical gelation). Between the sol–gel and MOD processes, a variety of chemical solution routes can be utilized for the preparation of the buffer and YBCO layer such as chelate processes, nitrate and citrate routes, and the pechini method. Common to all precursor solutions independent of the synthesis route used are a sufficient stability over time, an excellent wetting behavior on the desired substrate, and suitable rheological properties applicable to the chosen deposition technique (Knoth et al., 2006).

Two approaches are commonly used to complete the transformation of the as-deposited film into the crystalline ceramic: the two-step and the one-step processes.

In the two-step method, the as-deposited film is subjected to separate organic species through pyrolysis prior to crystallization at high temperatures. During the first step of the process, the film is typically placed on a hot plate held at 200–400°C for burnout of the organic species. Whilst it might be expected that this type of rapid

heat treatment would cause cracking, it appears that this is often the best approach. It has been proposed that this approach allows for the removal of the organic constituents prior to the collapse of the amorphous network, thus minimizing cracking and blistering. Films prepared from less reactive precursors retain their viscoelastic character longer during processing, and hence the solvent can be removed without producing significant stress.

In the one-step process, the film is heated directly to the crystallization temperature, which results in both organic removal and crystallization. Due to the 'single-step' nature of this approach and the use of relatively high temperatures (700–1200°C), a number of complex and potentially overlapping processes may occur during this one-step processing. A further complication in understanding these processes is the rapid heating rates (>100 K s^{-1}), which are frequently employed in the *one-step* process. These heating rates are typically achieved through the use of either rapid thermal annealing furnaces or by directly inserting the film into a furnace preheated to the crystallization temperature. Notwithstanding rapid heating rates are used, cracking in the films is typically not observed. Substrate, solution and material chemistry, transformation pathway, and thermal processing conditions all can have a significant effect on thin film microstructure and orientation.

The pyrolysed films are typically amorphous, film crystallization occurs by a nucleation and growth process. The theoretical description of nucleation and growth in solution-derived films is analogous to that used to describe crystallization in traditional glasses. The characteristics of the nucleation and growth process serve to define the resulting microstructure. To illustrate, films that display microstructures where only interface nucleation of the final crystalline phase takes place are frequently columnar in nature, whereas those in which nucleation occur throughout the film are typically polycrystalline with equiaxed grains. From a thermodynamic perspective it has been demonstrated that the driving forces that govern the transformation from the amorphous film into the crystalline ceramic can play an important role in defining the active nucleation

events, and thereby film microstructure. The diagram shown in Figure 3.2 demonstrates the differences in free energy between the solution-derived amorphous film and the crystalline ceramic phase. While this diagram does not necessarily provide insight into the transformation pathway the film undergoes, it is useful in understanding the role that the driving force (ΔG_V, the energy difference between the amorphous and crystalline states) can have on the transformation process and thus the final microstructure of the ceramic film. Examination of the figure indicates that the crystallization driving force is determined by the free energy of the two material states and the temperature at which crystallization occurs. The free energy of the amorphous phase is greater than the super cooled equilibrium liquid due to surface area, residual hydroxyl, and excess free volume contributions to the free energy. From standard nucleation and growth theory, the homogenous nucleation of a spherical crystallite in an amorphous film, the Gibbs free energy change is given by;

$$\Delta G_{\text{hom}o} = V(\Delta G_V + \Delta G_e) + A\gamma \tag{3.1}$$

where V, A, ΔG_v, ΔG_e, and γ are, the nuclei volume, the interfacial area between the nuclei and the parent amorphous phase, the difference in volume free energy, the elastic strain energy, and the interfacial energy of the newly formed interface respectively. By differentiation of above equation, the energy barrier for a stable homogenous nucleation event can be derived as,

$$\Delta G_{\text{hom}o}^* = \frac{16\pi\gamma^3}{3(\Delta G_V + \Delta G_e)^2} \tag{3.2}$$

The energy barrier to nucleation can decrease because of the internal or external surfaces or other defects. A nucleus formed in the shape of a spherical cap results in less of an increase in surface energy than homogeneous nucleation of a sphere of equivalent volume. The energy barrier to nucleation depends on surface tension forces. The relationship among these forces is given by,

$$\gamma_{sa} = \gamma_{ca} \cos\theta + \gamma_{sc} \qquad\qquad (3.3)$$

where the subscript "s" stands for substrate, "c" shows the crystalline nucleus, and a indicates the amorphous matrix.
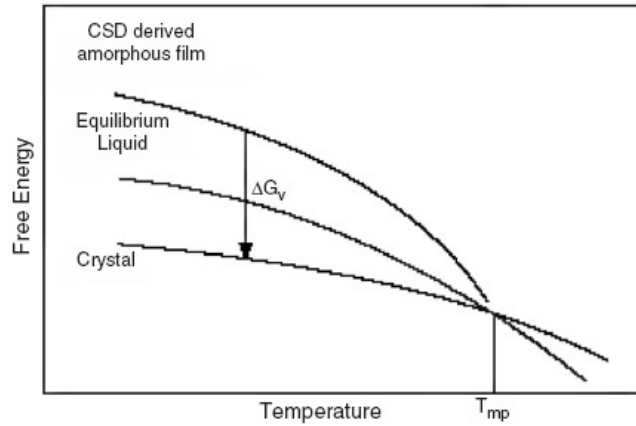

Figure 3.2 Schematic diagram of the free energies of a CSD-derived film (Bhuiyan, Paranthaman & Salama, 2006).

The initial surface energy of the heterogeneous nucleation site is γ_{sa}, and γ_{ca} and γ_{sc} are the newly created surface energies between the nucleus and the matrix and the nucleus and the substrate, respectively. The contact angle between γ_{ca} and γ_{sc} is θ. The energy barrier to nucleation is reduced in proportion to θ, and the nucleation is said to be heterogeneous. Strain energy effects can alter interfacial energies but now that these alternations cannot be verified by experiment, they are neglected in this simplified model. For $\theta \neq 0$, the heterogeneous nucleation barrier can be described by,

$$\Delta G^*_{hetereo} = \Delta G^*_{homo} f(\theta) = \frac{16\pi\gamma^3}{3(\Delta G_V + \Delta G_e)^2} f(\theta) \qquad\qquad (3.4)$$

where $f(\theta)$ is defined as,

$$f(\theta) = \frac{(2+\cos\theta)(1-\cos\theta)^2}{4} \qquad\qquad (3.5)$$

From Equation (3.5), it can be seen that the term $f(\theta)$, and thus the nucleation barrier, would disappear as the contact angle θ approaches zero. Nevertheless, crystallization under these conditions for standard solution processing routes is not observed due to the 'kinetic barrier' to crystallization. Although more detailed analyses are possible, only a few concepts are required to use the diagram in Figure 3.2 and the basic nucleation and growth equations to interpret film crystallization behavior. These are listed below.

i. As the crystallization driving force is increased, bulk nucleation becomes as probable as interface nucleation. In spite of the fact that the $f(\theta)$ term results in a lower energy barrier for interface nucleation, when the crystallization driving force is high (i.e., in a typical heat treatment scenarios) there is more than sufficient energy to surmount the energy barriers for all (including less energetically favorable) nucleation events.

ii. For films that transform with smaller driving forces, the energy barrier heights for different nucleation events are separated to a greater extent. This makes interface nucleation in some films much more preferred than bulk nucleation, and increases the importance of the substrate in influencing the thin film microstructure.

iii. The effects of crystallization temperature on driving force and nucleation must be considered. Upon using high heating rates, the physical processes leading to densification and crystallization of the film are delayed to higher temperatures. This causes nucleation to occur at a higher temperature than with conventional heating. Under these conditions, crystallization occurs with lower driving forces and due to the $f(\theta)$ term, lower energy heterogeneous nucleation events become more important.

iv. Unless rapid thermal processing techniques are used, film crystallization usually begins during heating to the annealing temperature. Therefore, as the temperature of the sample is increased more thermal energy becomes available to

surmount the barriers for nucleation events that are not necessarily the most favorable energetically. This can lead to film microstructures controlled by nucleation and growth processes associated with more than one nucleation event (Bhuiyan, Paranthaman & Salama, 2006).

3.1.1 Sol-Gel Process

Sol-gel process describes, in general, the formation of solid materials, mainly inorganic nonmetallic materials from solutions. This can be a solution of monomeric, oligomeric, polymeric or colloidal precursors.
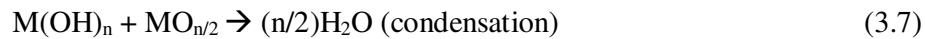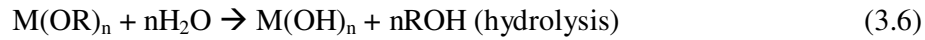
The sol-gel method of fabricating thin films offers potential advantages over traditional techniques as shown below:

  i. Low temperature processing,
 ii. Easy coating of large surface,
iii. Small thickness,
 iv. High optical quality,
  v. High purity.

The sol gel process consists of:

  i. Preparing a homogeneous solution of easily purified precursors generally in an organic solvent miscible with water or the reagent used in the next step,
 ii. Converting the solution to the 'sol' form by treatment with a suitable reagent, *e.g.* water with HCl for oxide ceramics,
iii. Allowing/inducing the sol to change into a 'gel' by polycondensation,
 iv. Shaping the gel (or viscous sol) to the finally desired forms or shape such as thin film, fiber, spheres or grains,
  v. Finally converting (sintering) the shaped gel to the desired ceramic material at temperatures (~500°C) generally much lower than those required in the conventional procedure of melting oxides together.

Usually, alkoxides are used as starting compounds, that is, organometallic substances of the form M $(OR)_n$ (M: metal of valence n, R: alkyl group C_xH_{2x+1}). By two groups of reactions, hydrolysis and condensation, the alkoxides are converted to three-dimensionally connected networks. More generally for an alkoxide of a metal M with valence n, the following reactions will take place;

$$M(OR)_n + nH_2O \rightarrow M(OH)_n + nROH \text{ (hydrolysis)} \qquad (3.6)$$

$$M(OH)_n + MO_{n/2} \rightarrow (n/2)H_2O \text{ (condensation)} \qquad (3.7)$$

$$M(OR)_n + (n/2)H_2O \rightarrow MO_{n/2} + nROH \text{ (overall)} \qquad (3.8)$$

The reactions in the sol-gel processes depend on many parameters, for examples:

    i. Compositions and concentrations of alkoxides and solvent used,
    ii. Amount of added water,
    iii. Catalyst used (type concentration),
    iv. Further additives: cheating substances such as diketones or desiccating controlling chemical additives (DCCA) such as NH_2CHO,
    v. Sequence in which the components are added,
    vi. Time schedule of mixing, for example aging (pre-hydrolysis) of components or intermediates that react slowly,
    vii. Further conditions of mixing *(e.g.,* mixing efficiency, surface-to-volume ratio, ultrasonic agitation, atmosphere),
    viii. Temperature.

To obtain a sol-gel derived coating on a transparent substrate with a high optical quality, the coating process should be carried out in a very clean room, the coating liquid has to be filtered and the substrate has to be cleaned properly (Attia et al., 2002).

3.1.2 Metal Organic Deposition (MOD) Process

In conventional metal organic deposition (MOD), a gel film is deposited onto a substrate using a coating solution and dried. The gel film is calcined and fired to become a superconducting film at ambient pressure. This MOD greatly reduces the production cost but rarely obtains high J_c over 1 MA.cm^{-2} (77 K, 0 T). Stable $BaCO_3$ distributes as a carboxylic group and reduces J_c of the YBCO films. More importantly, nucleation of nano crystallites in the precursor films causes YBCO grains to take on a random orientation during the firing process. It is difficult to obtain large area uniform high-J_c YBCO films with this process because the temperature and partial oxygen pressure must be simultaneously controlled precisely in order to decompose $BaCO_3$ entirely.

Araki et al. reported a version of MOD that enabled us to achive large-area uniform high-J_c YBCO film with high reproducibility. It is MOD using trifluoroacetates (TFA-MOD). In TFA-MOD, a fluorine-containing coating solution decomposes to fluorides in the precursor film and the fluorides cause very different chemical reactions during the following firing process compared with the conventional MOD. Consequently, high-J_c films on both large-area substrates and buffered metal substrates have been successfully formed by TFA-MOD. In TFA-MOD, impurities in the coating solution degrade the J_c of the resulting films. Highly purified coating solution was difficult to obtain in as much as hydrogen bonds between fluorine in trifluoroacetic acid and hydrogen in impurities in water and acetic acid disturb the refining process. Araki et al. developed a highly purified coating solution and obtained high-J_c films. Moreover, they confirmed that the purified solution had low sensitivity to the process conditions used to fabricate YBCO film. Whilst TFA-MOD is a kind of MOD, it has several characteristic features. Nano crystallites of the precursor film never influence the structure of the resulting YBCO film; the total firing time is simply proportional to the film thickness although it is generally proportional to the square of the thickness in conventional MOD; the obtained YBCO film has perfect orientation and harmful carbon content is entirely eliminated during the calcination process (Araki & Hirabayashi, 2003).

3.1.3 Pechini, Citrate and Nitrate Gel Route

In the Nitrate route the desired amounts of the nitrates are dissolved in deionized water or alcohol. Even though this approach is easier than the Pechini and Citrate methods a problem which can appear is the dewetting of the substrate. In the preparation of the citrate precursor solution in the Citrate route, stoichiometric amounts of metal nitrates are dissolved in water, and for the formation of the citrate compounds, citric acid is added. The precursor solutions in this method have a lower organic content and, in this way, the weight loss of the films during the transformation into the ceramic phase is lower. As starting substances for the Pechini route, metal nitrates are used. The metal nitrates are first dissolved in water, then citric acid, $HOC(COOH)(CH_2COOH)_2$, is added for the chelation of the cations resulting in the formation of a polybasic acid. Further, by adding a polyhydroxyalcohol, typically ethylene glycol, $HOCH_2CH_2OH$, the citric acid-metal chelates will react with ethylene glycol to form organic ester compounds. By heating the mixture the polyesterification and the formation of large metal/organic polymers occur. An advantage of this method is that the chemistry is well controlled. In this way, by varying the citric acid/ethylene glycol ratio and the solution preparation temperature, the viscosity and the polymer molecular weight of the solution can be controlled. The citrate route is similar to the Pechini route, except that the ethylene glycol and other polyhydroxy alcohols are not used (Apetrii, 2009).

CHAPTER FOUR
EXPERIMENTAL STUDY

4.1 Purpose

Among the different physical and chemical methods to prepare YBCO superconducting films, the metal organic decomposition method (MOD) has demonstrated major advantages, taking into account its versatility and low cost (Roma et al., 2006). YBCO is one of the most widely studied high temperature superconductor, thanks to its promising and attractive aspects of applications, which include energy storage systems, current limiters, magnetic bearings, etc., above liquid nitrogen temperature (77K). For these practical applications, it is desired to have high value of critical current density (J_c) even at higher applied magnetic fields. To improve the value of J_c, the flux line lattice needs to be strongly pinned by various crystal imperfections and the pinning force density has to be large. The pinning of flux line lattice in high temperature superconductors has been found to be weak, especially at higher temperatures and high magnetic fields. Therefore, in order to enhance the flux pinning strength, it is required to introduce artificial pinning centers in a superconductor apart from those which occur naturally. In order to enhance the J_c of thin films a novel technology has been developed by means of a nanostructure engineering to create artificial pinning centers in HTC materials (Jha & Khare, 2010). For this reason, in this study, improvement of flux pinning properties of YBCO superconducting films with $BaMeO_3$ (Me: Hf and Ir) perovskite nanoparticles are aimed by using TFA-MOD method.

Prior to deposition process, solution characteristics were performed to estimate further processing in TFA-MOD technique. The rheological properties of YBCO solutions were characterized through rheometer machine. In order to determine wetting angle between solution and substrate, contact angle measurements were carried out. For process optimization in TFA-MOD method, thermal, structural and morphologic studies were performed. Thermal behavior of gel was evaluated by differential thermal analysis-thermograviometry (DTA-TG) and fourier transform

infrared spectroscopy (FT-IR) was used for determination of organic complexes in dried powder. X-ray diffraction (XRD) was used to identify crystalline phases in YBCO based thin film. Surface chemistry of pure and doped YBCO thin films was characterized in favour of X-ray photoelectron spectroscopy (XPS). The surface topographies and morphologies of YBCO films were determined by using scanning electron microscope-energy dispersive spectroscopy (SEM-EDS). The morphological quality of the thin films was determined with the help of atomic force microscopy (AFM) device. The thickness of the films was measured by means of surface profilometer. As for electrical properties of the superconducting films, critical temperature and critical current density were scrutinized in this concept. Critical temperature and critical current density of pure and $BaMeO_3$ doped YBCO thin films were determined to identify dopant effects with the aid of JANIS SHI-4 Series 4.2K Cryostat.

4.2 Materials

4.2.1 Substrate Materials

Substrate material for high temperature superconducting thin films must fulfill the fundamental requirements. It must be thermally and chemically stable at the elevated temperatures which superconductor deposition is carried out. Additionally, there should not be any chemical interaction at the interface between coating and substrate. Differential thermal expansion of the substrate and superconductor film must be similar. If the substrate has a higher thermal expansion coefficient than the superconductor, it will contract more upon cooling from the deposition temperature, causing a compressive stress in the superconducting layer. For substrates with a lower thermal expansion, the superconductor will be in tension. Any stress may lead to a degradation of the film quality and subsequently the superconducting properties. Hence a substrate should ideally possess a thermal expansivity which is matched to, or slightly higher than superconducting film.

The surface of the substrate must be suitably polished, stable and reasonably robust. If the substrate surface is very rough, the superconductor will not be able to form a smooth, continuous well oriented film (Birlik, 2011).

(100) oriented commercial $SrTiO_3$ (STO) single crystal oxides from CrysTec GmbH Company with dimensions of 10 mm x 10 mm x 1 mm were utilized as substrates in order to prepare superconducting thin films. Proper preparation of STO substrate is the most important step in achieving a successful deposition process of all final coatings. Therefore it must be sound, clean, dust free and not be contaminated with oil, grease, paint, wax, curing compounds, or any such material that may act as a bond breaker. The key item being to create a good bond between the substrate and the superconducting films is surface preparation of STO substrates. Owing to these reasons, the substrate was cleaned in an ultrasonic bath using acetone in order to eliminate impurities from the sample surface.

4.2.2 Chemical Materials

In order to prepare YBCO based thin films, yttrium acetate ($Y(CH_3COO)_3.4H_2O$), barium acetate ($Ba(CH_3COO)_2$) and copper acetate ($Cu(CH_3COO)$) were used as precursor materials. Distilled water was utilized to dissolve precursors as a solvent. Trifluoroacetic acid (CF_3COOH) was used to synthesize dissolved precursors. The concentration of the solution was fixed to 0.25 M with addition of methanol (CH_3OH) as a diluting solvent. Hf (IV) 2.4 pentanedionate ($C_{20}H_{28}O_8Hf$) and Ir (III) pentanedionate ($C_{15}H_{21}IrO_6$) were utilized to incorporate into pure YBCO solutions as dopant materials.

4.3 Preparation of Solutions

One of the most important parameters in the MOD processing of coated conductor is the synthesis of MOD precursor solution. A flow chart for the solution synthesis process is illustrated in Figure 4.1 in detail.
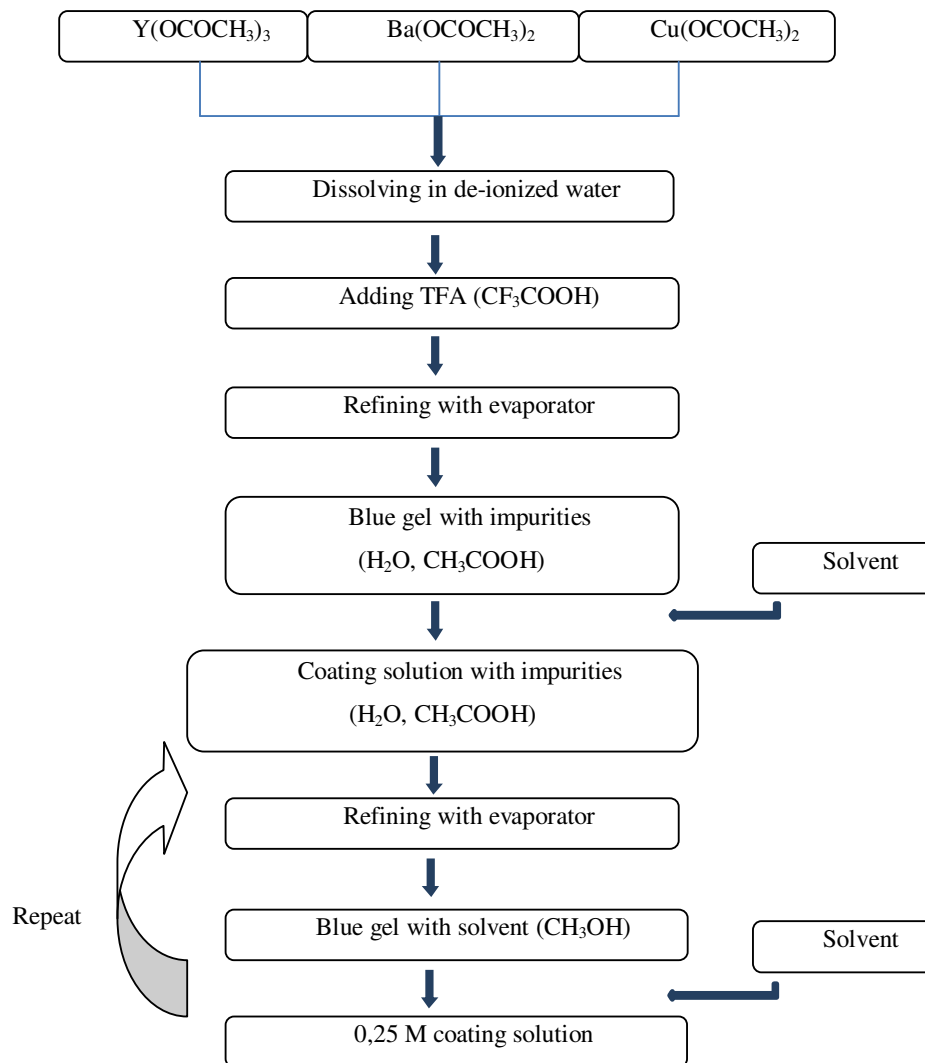
Figure 4.1. Schematic illustration of coating solution preparation by ytrium, barium and copper acetates.

The precursor solutions of pure and $BaMeO_3$ doped YBCO were prepared by dissolving acetates of Y, Ba and Cu into distilled water in a 1:2:3 cation ratio with arbitrary quantity of trifluoroacetic acid (TFA) at room temperature (10 ml TFA for 25 ml final solution). This aqueous solution was refined under vacuum atmosphere with evaporator in order to remove the solvent and to yield a glassy blue residue containing impurities of water and acetic acid. The experimental setup for evaporation is illustrated in Figure 4.2. Later, the residue was dissolved in sufficient methanol and refined again to expel the impurities to yield a glassy blue residue containing methanol. The concentration of the solution was fixed to 0.25 M with

addition of methanol with a certain ratio. Solution preparation process was adapted from the study executed by Birlik et al. (2010) with $BaZrO_3$ particles in the YBCO film structure.

Figure 4.2 Experimental setup for solution evaporation.

The final solution was divided into seven parts each 3 ml, and different amounts of hafnium and iridium were added to each part by dissolving Hf (IV)-2.4-pentanedionate and Ir (III) pentanedionate in the solutions. The Hf and Ir concentrations were adjusted to 0, 1, 3 and 5 mole %. The colour of the precursor solutions are varied as a function of dopant type and concentration from blue to dark green as shown in Figure 4.3.
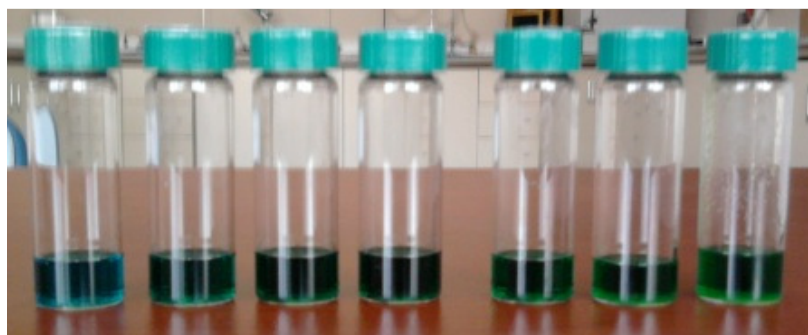

Figure 4.3 Picture of Hf and Ir added YBCO precursor solutions.

Table 4.1 summarizes the shortened names of precursor solutions and films prepared from these solutions. "Sol" and "F" represents solutions and films respectively.

Table 4.1 A brief summary which describes the solutions and the films prepared from these solutions.

Name of Solution	Type of Precursors	Type of solvents	Name of dopant precursors	Doped BHO and BIO concentration (mole %)	Name of film (STO substrate)
Sol-0	Y-ac Ba-ac Cu-ac		-	0	F-0
Sol-Hf-1	Y-ac Ba-ac Cu-ac			1	F(Hf-1)
Sol-Hf-3	Y-ac Ba-ac Cu-ac	Distilled water, TFA, Methanol	Hf(IV)-2.4-pentanedionate	3	F(Hf-3)
Sol-Hf-5	Y-ac Ba-ac Cu-ac			5	F(Hf-5)
Sol-Ir-1	Y-ac Ba-ac Cu-ac			1	F(Ir-1)
Sol-Ir-3	Y-ac Ba-ac Cu-ac		Ir (III) pentanedionate	3	F(Ir-3)
Sol-Ir-5	Y-ac Ba-ac Cu-ac			5	F(Ir-5)

4.4 Fabrication of Thin Films

Uniform gel films were obtained on $SrTiO_3$ (STO) single crystal substrate by spin coating. The substrate is located on the turntable with reduced pressure from vacuum

pump. The precursor films can easily absorb water. For this reason all coating process took place in a dry nitrogen atmosphere. Coating solution is dripped onto the substrate and rotation was started. Solvent swiftly vaporizes and gel film forms on the substrate. The schematic illustration of spin coating is shown in Figure 4.4.
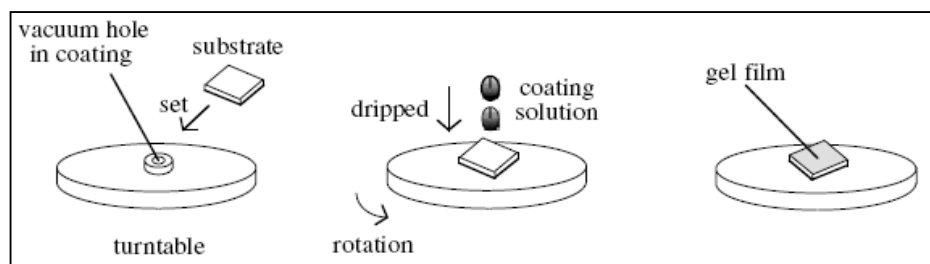

Figure 4.4 Schematic illustration of spin coating (Araki & Hirabayashi, 2003).

Final film thickness depends on the nature of the precursor solution as viscosity, drying rate and surface tension in addition to the parameters chosen for the spin coating process. Spin coating is a versatile deposition method allowing modification of the final film thickness through rotation speed control. Despite this, it may lead to inhomogeneous thickness at reduced rotation speeds. Thus YBCO superconducting thin films were produced by means of a high rotation speed of 6000 rpm and acceleration speed of 6000 rpm s^{-1} for 30 seconds.

The atmosphere controlled heat treatment system used in this study is shown in Figure 4.5. The atmosphere was controlled by using a computer program. The heat treatment recipe was adapted from the study which promoted by Obradors et al. (2004) and Birlik et al. (2010). They produced thin films which have a smooth, crack free surface and c-axis oriented grains. Figure 4.6 depicts heat treatment profile pure and BaMeO$_3$ doped YBCO films. All samples were heat treated according to this profile. For the first step, below 60°C, dry oxygen prevents the gel film absorbing humidity. If the gel film absorbs humidity, it will be corrupted. In second step, above 60°C, humidified O$_2$ was sent into the furnace to suppress the sublimation of Cu trifluoroacetate. During pyrolysis step metal trifluoroacetates decompose and harmful gaseous residues are removed. After that, the temperature was increased to

780^oC for the crystallization under humidified N_2 with 100 ppm O_2. The final superconducting films were obtained after oxygenated at 450^oC (Birlik, 2011).

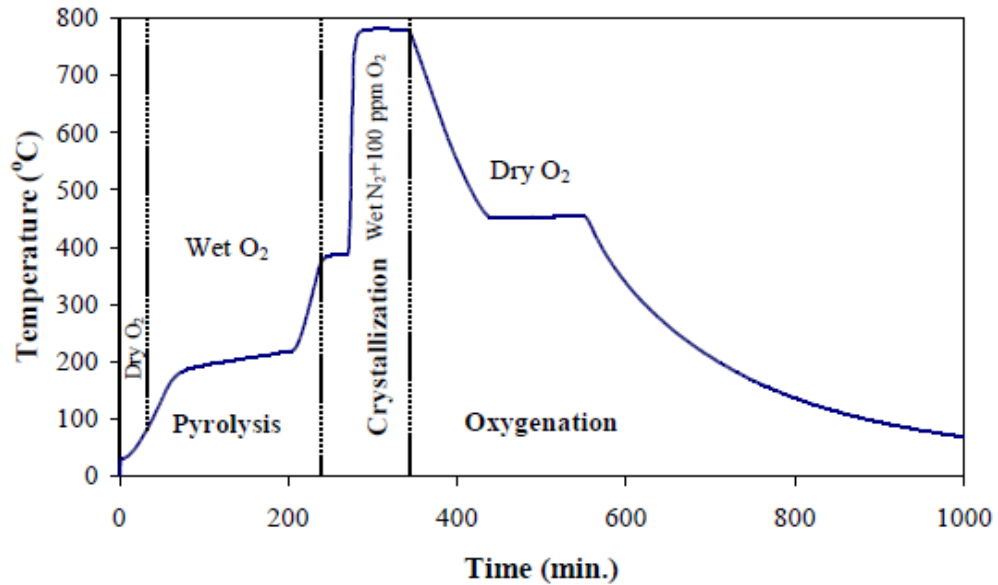Figure 4.5 Atmosphere controlled heat treatment system.

Figure 4.6 Heat treatment profile for the production of pure and $BaMeO_3$ doped YBCO films. All films are crystallized at 780^oC and oxygenated at 450^oC (Birlik, 2010).

Images of smooth and crack free surface profiles for pure and BaMeO$_3$ doped YBCO thin films on STO substrates are shown in Figure 4.7. These images of YBCO based films on STO substrate were taken after heat treatment process.
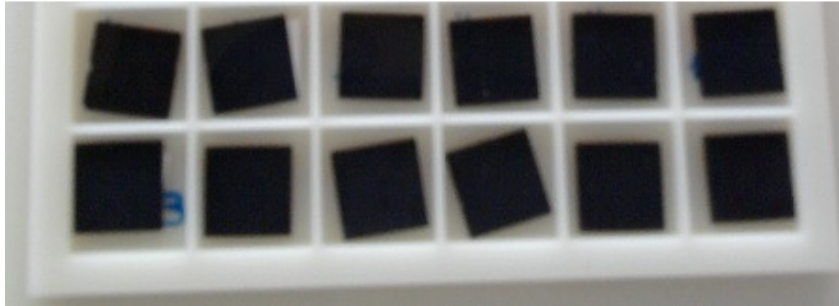

Figure 4.7 Images of smooth and crack free surface profiles for pure and BaMeO$_3$ doped YBCO thin films on STO substrate.

4.5. Solution Characterization

4.5.1 Rheology Measurement

Rheology is the science of flow and deformation of matter under the influence of an applied stress (shear stress or tensile stress) and describes the relation among force, deformation and time. Fluid rheology is used to describe the consistency of different products, normally by the two components: viscosity and elasticity. Viscosity is the measure of a material's resistance to flow. It is a material property which depends on different parameters such as: mechanical stress and strain, time, as well as temperature and other ambient conditions. In rheology it is distinguished between so-called Newtonian and non-Newtonian materials. Newtonian materials are characterized by a viscosity which may depend on the temperature but is independent of the shear rate (and shear stress). In contrast, the viscosity of the non-Newtonian materials depends on the shear rate.

Friction becomes apparent when a layer of fluid is forced to move in relation to another layer. The greater the friction, the greater the amount of force required to cause this movement, which is called shear. Shearing occurs whenever the fluid is

physically moved or distributed, as in pouring, spreading, spraying or mixing. Isaac Newton defined viscosity by considering the model represented in Figure 4.8.
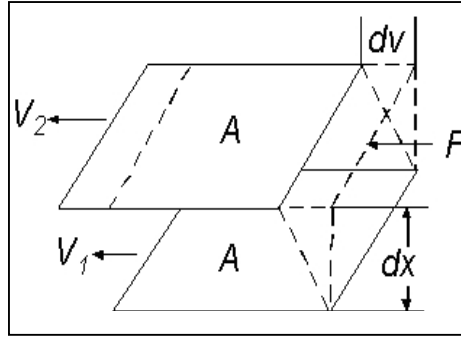

Figure 4.8 Definition of shear stress and shear rate based on shearing between planes

Two parallel planes of fluid of equal area A are separated by a distance dx and are moving in the same direction at different velocities V_1 and V_2. Newton assumed that the force required maintaining this difference in speed was proportional to the difference in speed through the liquid, or the velocity gradient. The velocity gradient, dv/dx, is a measure of the change in speed at which the intermediate layers move with respect to each other. It describes the shearing, which the liquid experiences, and is thus called shear rate. The shear stress is defined as:

$$\tau = F / A, \quad F: \text{force (N)}, \quad \text{and A: area (m}^2) \tag{4.1}$$

The shear rate is defined as:

$$\gamma = dv / dx \tag{4.2}$$

Owing to the necessity to control the stability of the precursor solution the dynamic viscosity was measured:

$$\eta = \tau / \gamma \quad ; \quad [\eta] = \text{Pa.s}, \tag{4.3}$$

in which η is the dynamic viscosity. The flow curve, which is a plot of shear stress versus shear rate, will, therefore, be a straight line with slope η for a Newtonian fluid (Apetrii, 2009).

Once a sol or solution transforms to a gel, gelation occurs. Cross-linking reactions are able to connect macromolecules into a tridimensional polymeric network. During the initial stages of the cross-linking process, branched molecules of widely distributed sizes and of various architectures are formed. Their average molecular weight increases with increasing extend of cross-linking reaction, p. The system reaches its gel point (GP) at a critical extent of reaction ($p=p_c$) at which either the weight-average molecular weight diverges to infinity or a first macromolecular cluster extends across the entire sample. Consequently, the system loses its solubility, the steady-shear viscosity diverges to infinity, and the equilibrium modulus starts to rise to a finite value. The newly formed macroscopic network structure starts to coexist with the remaining branched molecules which are not yet attached (Winter, 1987).

The rheological measurements were conducted with the help of a Bohlin Instruments CVO 100 Rheometer with 2° conic plate geometry, 60 mm in diameter and 70 μm gap sizes between plates. The viscosity values of precursor solutions were determined at 25^oC at single shear mode and under increasing temperature conditions at constant 400 Hertz between 25-60°C for all solutions. In addition gel-point of profiles for pure and $BaMeO_3$ doped precursor solutions was determined at 60^oC. The gel-point is described by taking a time which gelation realizes during deposition process.

4.5.2 Contact Angle

The contact angle is the angle at which the liquid/gas interface meets the solid interface. This characteristic behavior is described in Figure 4.9. Assuming that the solid surface is perfectly smooth it is easy to show that the system has to obey to the following equation, called Young equation;

$$\gamma_{SV} + \gamma_{SL} = \gamma_{LV} \cdot \cos \gamma \tag{4.4}$$

where γ_{SL} is solid–liquid, γ_{LV} is liquid–vapor and γ_{SV} solid–vapor interfaces.
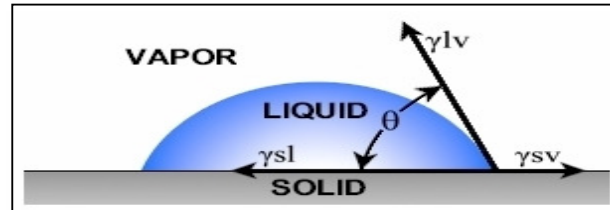

Figure 4.9 The schematic view of contact angle.

A change in the surface structure due to a re-arrangement of its molecules or to the interaction with the environment can be hard to detect with a microscope, but it is easily detectable through a contact angle measurement. This is because the structure change strongly influences the surface energy and consequently the contact angle. It is in this case that contact angle measurements are used (Campanini, 2011). In order to obtain a complete homogenous coverage of the STO single crystal substrates, a very small wetting angle close to $0°$ was required.

Contact angle measurements of the precursor solutions were performed to estimate their wettability properties with Contact Angle Meter-CAM 100 (KSV Instruments Ltd., Finland). It is a compact CCD camera based instrument for measurement of contact angles of liquids on solids. Goniometry involves the observation of a sessile drop of test liquid on a solid substrate. The basic elements of a goniometer include a light source, sample stage, lens and image capture. Contact angle can be evaluated directly by measuring the angle formed between the solid and the tangent to the drop surface. After measuring the contact angles of the precursor solutions, their values gives about film qualities obtained in further processing of MOD-TFA technique.

4.6. Material Characterization

4.6.1 Differential Thermal Analysis-Thermogravimetry (DTA-TG)

The most widely used thermal method of analysis is differential thermal analysis (DTA). In DTA, the temperature of a sample is compared with that of an inert reference material during a programmed change of temperature. The temperature should be the same until thermal phenomenon occurs, such as melting, decomposition or change in the crystal structure. In an endothermic phenomenon takes place within the sample, the temperature of the sample will lag behind that of the reference and a minimum will be observed on the curve. On the contrary, if an exothermal phenomenon takes place, then the temperature of the sample will exceed that of the reference and a maximum will be observed on the curve. The area under the endotherm or exotherm is related to the enthalpy of the thermal event, ΔH.

Thermogravimetry (TG) measures the change in mass of a material as a function of time at a determined temperature (i.e., isothermal mode), or over a temperature range using a predetermined heating rate. Essentially, a TG consists of a microbalance surrounded by a furnace. A computer records any mass gains or losses. Weight is plotted against a function of time for isothermal studies and as a function of temperature for experiments at constant heating rate. Thus, this technique is very useful in monitoring heat stability and loss of components (Ramachandran, Paroli, Beaudoin & Delgado, 2002).

Thermal behavior of xerogels, which were dried at $100^{o}C$ for 3 hours in air, was evaluated using DTA/TG machine (DTG-60H Shimadzu) to gain solution evaporation, decomposition and phase formation and to obtain an optimum heat treatment regime for drying, heat treatment and annealing processes. Prior to performing DTA-TG measurement of the xerogels, they were weighted as approximately 20 mg and then put into crucible. In these experiments, Al_2O_3 powder with 60 μm was used as a reference material. The experiments were conducted under

N_2 flow in the temperature range from ambient to 800°C at a heating rate of 10°C/min.

4.6.2 Fourier Transform Infrared Spectroscopy (FT-IR)

FT-IR stands for Fourier Transform Infrared, the preferred method of infrared spectroscopy. In infrared spectroscopy, IR radiation is passed through a sample. Some of the infrared radiation is absorbed by the sample and some of it is passed through (transmitted). The resulting spectrum represents the molecular absorption and transmission, creating a molecular fingerprint of the sample.

Infrared spectroscopy has been a workhorse technique for materials analysis in the laboratory for over seventy years. An infrared spectrum represents a fingerprint of a sample with absorption peaks which correspond to the frequencies of vibrations between the bonds of the atoms making up the material. Because each different material is a unique combination of atoms, no two compounds produce the exact same infrared spectrum. Therefore, infrared spectroscopy can result in a positive identification (qualitative analysis) of every different kind of material. In addition, the size of the peaks in the spectrum is a direct indication of the amount of material present. With modern software algorithms, infrared is an excellent tool for quantitative analysis (Thermo Nicolet Corporation, 2001).

Fourier transform infrared spectroscopy (FT-IR) was used for determination of organic compounds/complexes in xerogel powders. For these experiments, pure and BHO and BIO doped precursor solutions were dried at 200°C for 3 hours in air. FT-IR (Perkin Elmer) absorption spectra were measured over the range of 4,000–650 cm^{-1} at room temperature in air. In this study, variations of concentration organic components/complexes depending on temperature were determined by Perkin–Elmer Fluka library. By interpreting the FT-IR spectra of the xerogel powders, the chemical bonds in a molecule were determined after the measurements.

4.6.3 X-Ray Diffraction (XRD)

XRD is a powerful technique used to uniquely identify the crystalline phases present in materials and measure the structural properties (strain state, grain size, epitaxy, phase composition, preferred orientation and defect structure) of these phases. XRD is non-contact and non-destructive. The regular array of atoms in a crystalline material forms a 3D diffraction grating for waves with a wavelength around that of the distance between the atoms. When waves enter a crystal, they are scattered in all directions by the atoms. In certain directions, these waves can interfere destructively. In other directions, constructive interference will occur resulting in peaks in X-ray intensity. The diffraction pattern that results is a map of the reciprocal lattice of the crystal and can be used to determine the structure of the crystal. Bragg's law is the basis for crystal diffraction:

$$n.\lambda = 2.d.\sin\theta \qquad\qquad (4.5)$$

where n is an integer known as the order of diffraction, λ is the X-ray wavelength is the spacing between two consecutive scattering planes and θ is the angle between the atomic planes and the incident (and diffracted) X-ray beam (Ahmed & Jackson, 2009). Figure 4.10 illustrates diffraction of x-rays by planes of atoms.
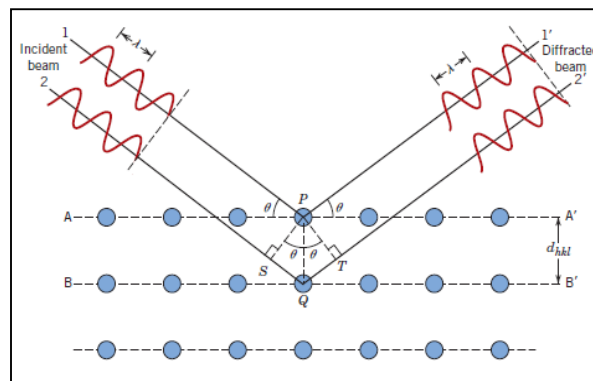

Figure 4.10 Diffraction of x-rays by planes of atoms (A–A` and B–B`) (Callister, 2007).

Bragg's law is necessary but not sufficient condition for diffraction by real crystals. It specifies when diffraction will occur for unit cells having atoms positioned only at cell corners. Nonetheless, atoms situated at other sites (e.g., face and interior unit cell positions as with FCC and BCC) act as extra scattering centers, which can produce out-of-phase scattering at certain Bragg angles. The net result is the absence of some diffracted beams that, according to Bragg´s law, should be present.

Schematic diagram of an X-ray diffractometer is presented in Figure 4.11. The diffractometer is an apparatus used to determine the angles at which diffraction occurs for specimens. A specimen S in the form of a flat plate is supported so that rotations about the axis labeled O are possible; this axis is perpendicular to the plane of the page. The monochromatic x-ray beam is generated at point T, and the intensities of diffracted beams are detected with a counter labeled C in the figure. The specimen, x-ray source, and counter are all coplanar (Callister, 2007).
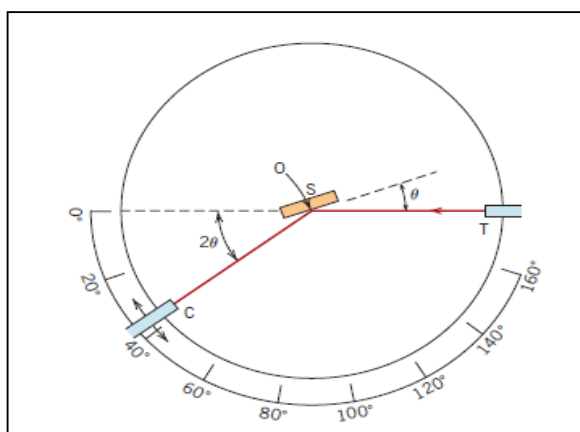
Figure 4.11 Schematic diagram of an x-ray diffractometer; T = x-ray source, S = specimen, C = detector, and O = the axis around which the specimen and detector rotate (Callister, 2007).

The crystal characteristic and structural development of the produced YBCO based superconducting thin films was investigated by XRD (Rigaku D/MAX-2200/PC) patterns, which was recorded using Cu K_α irradiation (wavelength, $\lambda = 0.15418$ nm) and the scanning range was between $2\theta = 10$ and 90°. A step scan with a step size of $0.02°$ and a counting time of 1 s/step was used.

4.6.4 X-Ray Photoelectron Spectroscopy (XPS)

When excess electromagnetic energy is transferred to an electron that is in a further out shell, it is called an Auger electron. An analysis of these for chemical identification is known as Auger electron spectroscopy (AES). X-ray photoelectron spectroscopy (XPS) analyses electron emission of similar high energy. XPS can be used to measure the chemical or electronic state of surface elements, detect chemical contamination or map chemical uniformity of YBCO based surfaces on STO substrates.

For XPS the material to be examined is irradiated with aluminum or magnesium X-rays. Monochromatic aluminum K_α X-rays are normally produced by diffracting and focusing a beam of non-monochromatic X-rays off of a thin disk of crystalline quartz. Such X-rays have a wavelength of 8.3386 Å, corresponding photon energy of 1486.7 eV and provide a typical energy resolution of 0.25 eV. Non-monochromatic magnesium X-rays have a wavelength of 9.89 Å, a corresponding photon energy of 1253 eV and a typical energy resolution of 0.90 eV. The kinetic energy of the emitted electrons is recorded. This kinetic energy of the ejected electrons is directly related to the element-specific atomic binding energy of the liberated. A plot of these energies against the corresponding number of electron counts provides the spectrum which indicates the qualitative and quantitative elemental composition. At these higher energies, XPS analyses only to a depth of 10 nm into the surface. Electrons emitted at greater depths are recaptured or trapped in various excited states within the material. Spectral profiles up to 1 μm deep can however be obtained by continuous spectral recording during ion etching or from consecutive ion etching and XPS measurement steps.

XPS is usually performed in ultra-high vacuum (UHV) and typically provides resolutions down to 1000 ppm. With optimum settings and long recording times, resolutions down to 100 ppm can be achieved. Non-monochromatic X-ray sources can produce a significant amount of heat (up to 200°C) on the surface of the sample as the anode producing the X-rays is typically only a couple of centimeters from the

sample. This level of heat when combined with high energy Bremsstrahlung X-rays can degrade the surface. Organic chemicals are therefore not routinely analyzed by non-monochromatic X-ray sources (Ahmed & Jackson, 2009).

Surface chemistry of pure and $BaMeO_3$ doped YBCO thin films were characterized by means of Thermo Scientific K-Alpha XPS system. Photoemission of electrons was produced using a monochromatic Al K_α X-ray source (1486.6 eV) operated at 150 W. The photoelectrons were allowed to pass through a hemispherical analyzer operated in fixed retardation ratio mode at 11.75 eV of pass energy. This results in an energy resolution of ≤ 0.51 eV. All data were acquired with take-off angle α of the detected electrons ranging from 30° to 70°. Note here α is defined with respect to intersection of the surface and the plane of incidence, viz. $\alpha = \pi/2 - \phi$, where ϕ is the polar angle defined with respect to the surface normal. The 30°-spectra would carry more of the signature of the chemical shifts of the surface reconstructed atoms or any other contaminants.

4.6.5 Scanning Electron Microscopy (SEM)/Energy Dispersive Spectroscopy (EDS)

Scanning electron microscopes (SEMs) have been used by researchers since 1935 to examine micrometer scale structures and more often recently to examine nanoscale structures. This is a versatile technique with which relatively large samples can be visualized, dimensional measurements can be taken and compositional analysis can be performed. The SEM works by initially firing primary electrons at the sample to be imaged. Electrons are dislodged from the atoms at the surface of the sample and are attracted to a positively charged detector grid. These electrons are known as secondary electrons. When a set pattern of primary electron beam scanning is used over the surface, recording of the secondary electrons allows the surface topology to be interpreted and displayed. Spatial resolution within a given SEM depends on the primary electron beam spot size and the volume of material with which the electrons interact. Under good conditions, such as high accelerating voltage (e.g. 30 kV), well-aligned apertures, well-corrected astigmatism, small spot

size (small probe current) and no sample charging, resolutions of 3 nm can typically be achieved. Conventionally, tungsten and carbon elements were used in SEMs; to achieve longer gun lives, LaB_6 elements have been adopted more recently. Primary electrons that are bounced back off the surface are known as back scattered electrons (BSE). The energy of these electrons is directly related to the density of the atoms from which they are repelled and therefore their recording allows the variation of surface composition to be visualized (Brabazon & Raffer, 2009). Figure 4.12 illustrates the basic elements of SEM device.
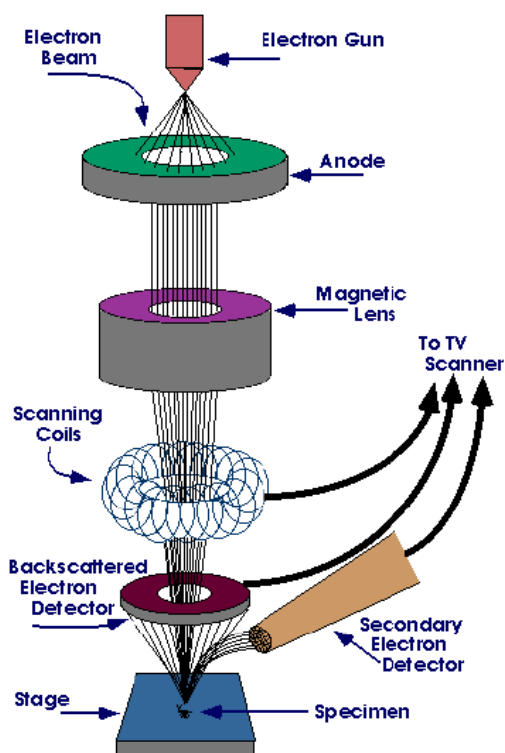
Figure 4.12 Schematic representation of SEM device (Vandaele, 2011).

The surface qualities, topographies and morphologies of pure and $BaMeO_3$ doped YBCO superconducting thin films on STO substrates were examined by using SEM (JEOL JSM 6060). Accelerating voltage of 20 kV was used for the SEM imaging and EDS analyses.

4.6.6 Atomic Force Microscope (AFM)

The atomic force microscope (AFM), also called the scanning force microscopy (SFM), was developed in 1986. The AFM involves scanning a sharp tip across a sample surface while monitoring the tip–sample interaction to allow the reconstruction of the 3D surface topography. A typical AFM has nanometer lateral and sub-angstrom vertical resolution and can image insulators as well as conductors. An AFM consists of a sharp tip at the end of a flexible cantilever which is moved across a sample surface by piezoelectric actuators. The cantilever is typically made from Si or Si_3N_4 with a tip curvature radius of a few nanometers. Displacement of the tip is recorded by a non-contact laser displacement measurement. A laser light directed onto the cantilever above the laser tip is recorded on a photo detector area which allows calculation of displacement via signal strength measurement or triangulation. A feedback loop maintains a constant tip–surface interaction force by vertically moving the scanner to maintain a constant photo detector difference signal. The distance the scanner moves vertically is recorded and with each *x*, *y* position which allows the surface information to be presented and analyzed. A complicated set of forces can be present at the tip–sample interaction. For a surface under ambient conditions, once the tip touches the surface a repulsive force is present with the tip at a small distance from the surface attractive forces can be present as well as van der Waals force and capillary force arising from condensation of water vapor in the contact area. Operating modes can be roughly classified as contact, non-contact and dynamic.

In contact mode, the scanning tip is dragged across the sample surface and the tip deflection is monitored. Using Hook's law, the force between the tip and the surface is automatically kept constant during scanning (typically between 0.1 and 100 nN). Lower stiffness cantilevers (spring constant, *k*<0.1 N/m) are used in this mode to amplify the deflection signal. Contact mode may not be suitable for soft materials which can be easily deformed or damaged, such as for polymer or molecular imaging. When scanning is performed in the region where the tip is attracted to the surface, the scanning is termed non-contact mode. In this region, the cantilever bends towards the sample. If an oscillatory tip displacement is sufficiently large to pass

through both regions, the probe experiences both attractive and repulsive forces. This mode is known as dynamic, intermittent or tapping mode. Tapping mode was developed for investigation of soft materials. In this mode, the cantilever oscillates near its resonant frequency and lightly taps the surface during scanning. The tip rapidly moves in and out of the sample surface with amplitude which is sufficiently high to overcome adhesion forces so that it stays in contact only for a short fraction of the oscillation period. Depending on the cantilever type, the frequency typically varies from 50 to 500 kHz and amplitudes up to 100 nm are used. The laser spot deflection is used to measure the amplitude of cantilever oscillation and a feedback loop maintains constant oscillation amplitude by adjustments to the servo which adjusts the cantilever height. In addition to the favorable imaging conditions and high resolution, the AFM offers a variety of new contrast mechanisms which can be used to provide information on differences in sample friction, adhesion, elasticity, hardness, electric fields, magnetic fields, carrier concentration, temperature distribution, spreading resistance and conductivity (Ahmed & Jackson, 2009).

Inasmuch as the AFM are used to more fully characterize the surface morphology and roughness of the superconducting thin films, their two and three dimensional surface characteristics was examined with the aid of Nanosurf Easyscan II AFM device.

4.6.7 Film Thickness Measurement

Surface Profilometer is a measuring instrument used to measure a surface profile of the films, in order to quantify its roughness and thickness. While the historical notion of a profilometer was a device similar to a phonograph that measures a surface as the surface is moved relative to the contact profilometer's stylus, this notion is changing with the emergence of numerous non-contact profilometery techniques. After obtaining optimum superconducting films, half of the thin films was etched and removed from substrate surface to measure their surface profiles and thicknesses. The step height from substrate to the films is a value for film thickness.

The thickness of the films was determined through Ambios Technology XP-2 Surface Profilometer.

4.7. Electrical Characterization

In the present work, the electrical properties (T_c, J_c and B_c) of the superconducting thin film samples were studied by using standard four probe method.

4.7.1 Critical Transition Temperature (T_c) Measurement

The critical transition temperature of the YBCO based thin films was determined under croyogenic conditions bearing liquid helium by using Physical Property Measurement System (PPMS) (Inonu University, Scientific and Technological Research Center) under zero magnetic fields. In that a four probe method is one of the standard and most widely used method for the measurement of resistivity of superconductors, it was applied to prepare YBCO based specimens before the transition temperature measurements of the thin films. The Ag paste was utilized to provide four contacts on the superconducting films on STO substrates.

Figure 4.13 schematically presents a curve of resistance versus temperature for a composite superconductor. A tangential line to a part of curve in the normal state region can be drawn. The value of temperature at the intersection of the transition curve and a line with 50% height of the tangential line (50% resistance) is determined as T_c. Two temperature values at the intersections of the transition curve and two lines with 10% and 90% heights of the tangential line are denoted by $T_{c0.1}$ and $T_{c0.9}$, respectively, as shown in Figure 4.14. The transition width, ΔT_c, is defined as $T_{c0.9}$- $T_{c0.1}$. ΔT_c shall be less than 3% of T_c.
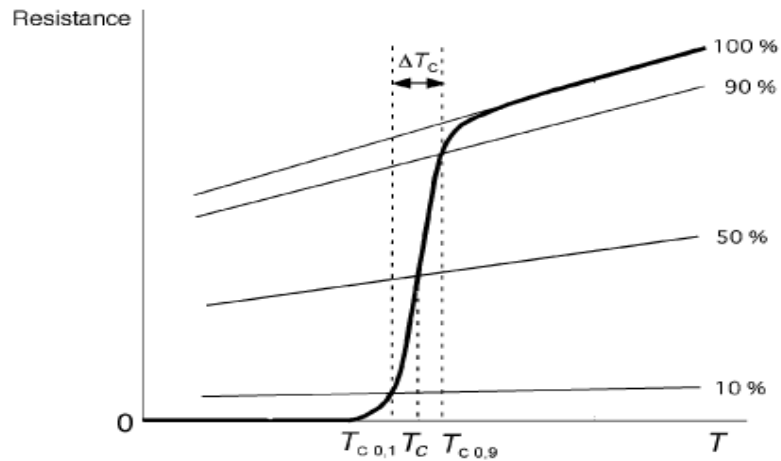
Figure 4.13 Determination of critical temperature (T_c) of a superconductor material (Murase et al., 2001)

4.7.1 Critical Current Density (J_c) and Critical Magnetic Field Measurements

Several methods exist for measuring critical current, but the most practical technique is the transport method. With the transport method, a current I is passed through the sample and the electric-potential difference (voltage) V is measured along its length. Ideally, the superconductor V–I characteristic should be highly nonlinear. As illustrated in Figure 4.14, at low transport current the superconductor has effectively zero resistance, but, at a critical value of current I_c, the voltage rapidly rises as the superconductor reverts to the normal resistive state. Ultimately, the transport method is the most trusted for determining I_c, but it requires care with current handling and contacts. On the other hand, indirect methods for determining I_c include magnetization measurements and eddy-current testing. These indirect methods are contactless techniques, in which current is electromagnetically induced in the sample, where it circulates within grains or small regions of the sample rather than along the entire sample length. Such contactless measurements are useful in the initial stages of characterizing new superconducting materials and production line testing for quality assurance.
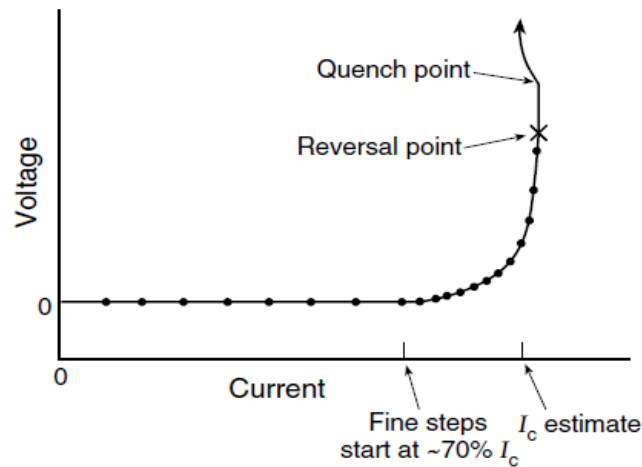
Figure 4.14 Plot of voltage vs. current for a typical superconductor, showing regions of negligible resistance (at lower currents), the highly nonlinear critical-current regime, and the quench point where thermal runaway occurs (Ekin, 2006) .

To make an equitable comparison between different superconductors, we divide the critical current by the cross-sectional area A of the conductor; this defines a critical-current density (Ekin, 2006);

$$J_c = I_c /A \qquad\qquad (4.9)$$

The critical current density (J_c) of the YBCO based thin films was determined by using PPMS. The critical magnetic field (B_c) values of pure and BaMeO$_3$ doped YBCO thin films were measured at 77K in up to 9T magnetic field by using same PPMS device (Inonu University, Scientific and Technological Research Center). All measurements were performed by standard four probe method and using silver paste contact. The voltage criterion for the J_c measurement was 50 µV/cm. The thin films in the form of square shape having 10 mm length, 10 mm width and 1 mm thickness, and 200-250 nm thickness were used for the J_c measurements.

CHAPTER FIVE
RESULTS AND DISCUSSION

5.1 Solution Characterization

5.1.1 Rheological Properties

Rheological characterization of YBCO based precursor solutions was performed to determine shear profile and temperature effect on their viscosity. The focus of attention here is mainly on the rheological properties in film production. The viscosity values of precursor solutions were determined at 25°C in air at single shear mode under standard conditions and 2 hours with a constantly increasing shear rates.

Rheological properties of pure, Hf and Ir added YBCO precursor solutions were demonstrated in Figures 5.1, 5.2 and 5.3. Regarding as rheological properties of the precursor solutions, viscosity measurement of undoped and BHO/BIO doped YBCO solutions were carried out at room temperature and increasing shear rate, at increasing temperature in the range of 25°C and 60°C and constant shear rate. Additionally, modulus measurements such as viscous and elastic modulus of the solutions were performed to anticipate their gel point values.

The instantaneous viscosity versus time graph of Hf added YBCO solutions at 25°C constant temperature are given in Figure 5.1a. Note that viscosity values of Sol-0, Sol-Hf-1, Sol-Hf-3 and Sol-Hf-5 (Hf added) solutions are low at low shear rates, but at high shear rates their viscosity values increase and stay nearly constant. It is obvious from these results that, viscosity values of all solutions are very close to each other. It should be noted that Hf additives to YBCO precursor solution slightly influence their viscosities. Figure 5.1b shows the viscosity shifts of Hf added solutions depending on processing temperature. For all solutions, at first viscosity value decreases with increasing temperature due to evaporation of solvent in the solutions, but then they reach a constant value. For Sol-Hf-5 the viscosity shift is huge as can be seen in the graph. It is clear from Figure 5.1 that the mean viscosity
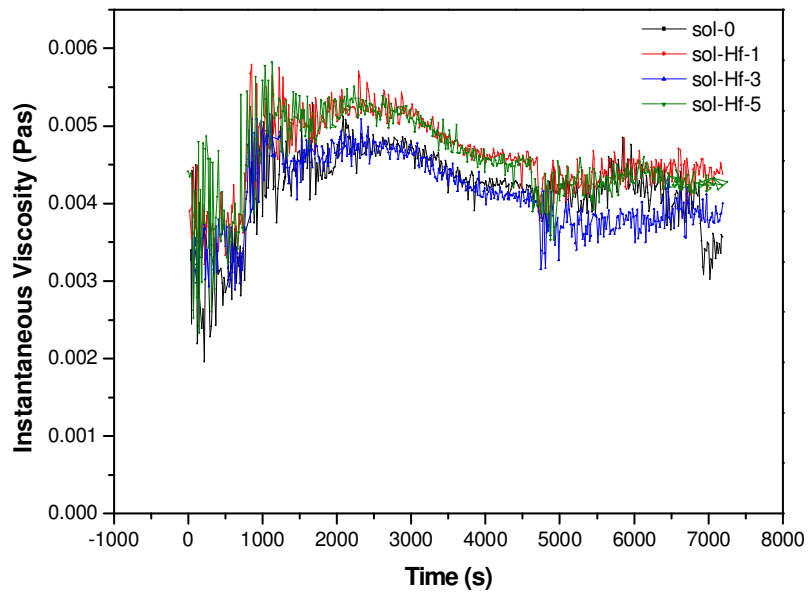
(a)
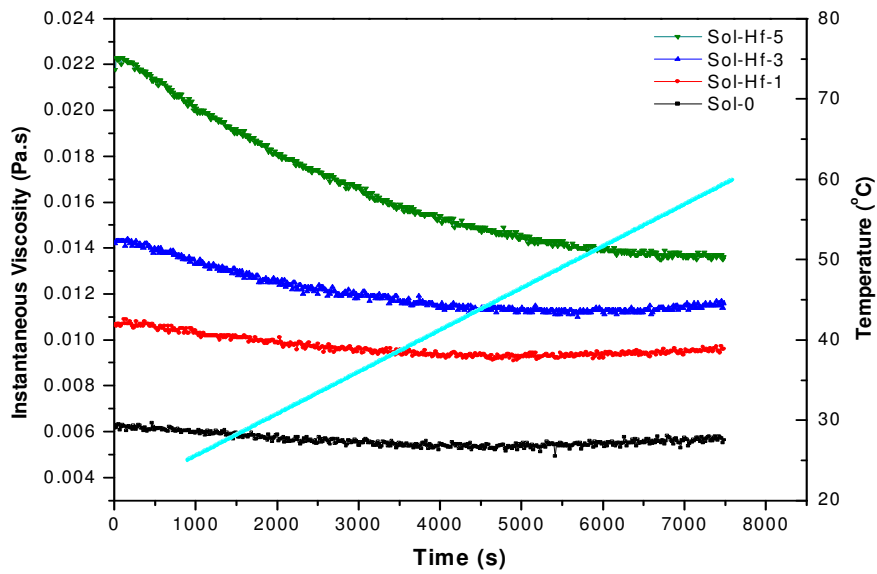
(b)

Figure 5.1 Viscosity measurement of undoped and BHO doped YBCO solutions (a) at room temperature and increasing shear rate and (b) at increasing temperature (25-60°C) and constant shear rate.

values are 4.19, 4.62, 4.13 and 4.29 mPa.s for Sol-0, Sol-Hf-1, Sol-Hf-3 and Sol-Hf-5 respectively. These viscosity values are quite likely to be a key factor for developments of the solutions and thin films. Due to this reason, these values present beneficial effects in thin film production.

Figure 5.2a denotes the variation of viscosity with increasing shear rate for Sol-0, Sol-Ir-1, Sol-Ir-3 and Sol-Ir-5 (Ir added) solutions at $25^{o}C$ constant temperature. It was found that the viscosity value of solutions is nearly the same except Sol-Ir-3. However, the difference between the viscosity values is very small. Therefore it will not affect the film structure and thickness. The instantaneous viscosity versus temperature graph of undoped and Ir added solutions are given in Figure 5.2b. Essentially, the same results were obtained for Ir added solutions. At first their viscosity decreases until $45^{o}C$, after that they reach a constant value. This is because solvent evaporated from precursor solutions. It is worth noting that the mean viscosity values are 4.19, 5.19, 11.63 and 3.54 mPa.s for Sol-0, Sol-Ir-1, Sol-Ir-3 and Sol-Ir-5, respectively. Compared to Hf added solutions, it can be expressed that similar results are obtained. These values are in the recommended levels for thin film deposition.

As mentioned in Chapter 4, Newtonian materials are characterized by a viscosity which may depend on the temperature but is independent of the shear rate (and shear stress). The viscosity of the non-Newtonian materials depends on the shear rate. Based on these viscosity results, undoped and doped YBCO solutions are Newtonian materials and their viscosity only depend on the processing temperature.

The gel-point values of undoped and 5 mole % Hf and Ir added YBCO precursor solutions are shown in Figures 5.3a, 5.3b and 5.3c. Time of gelation can be determined for all solutions. Viscous and elastic moduli can be changed depending on time for our cases. The time necessary to reach the intersection depends on the viscous and elastic moduli oscillations. Thus, this intersection could be used to define the experimental gel point. It can be noticed from Figure 5.3 that in spite of the fact that gelation time values of S-0 and S-Hf-5 solutions were 6850 sec. and

8400 sec. respectively, that of S-Ir-5 was found to 9800 sec. which is very long period. On the account of the fact that a very long gelation time is desirable during TFA-MOD processing in practical applications, these values are being made to harmonise solution preparation and to finalize well-textured, continuous superconducting thin films on STO substrates.
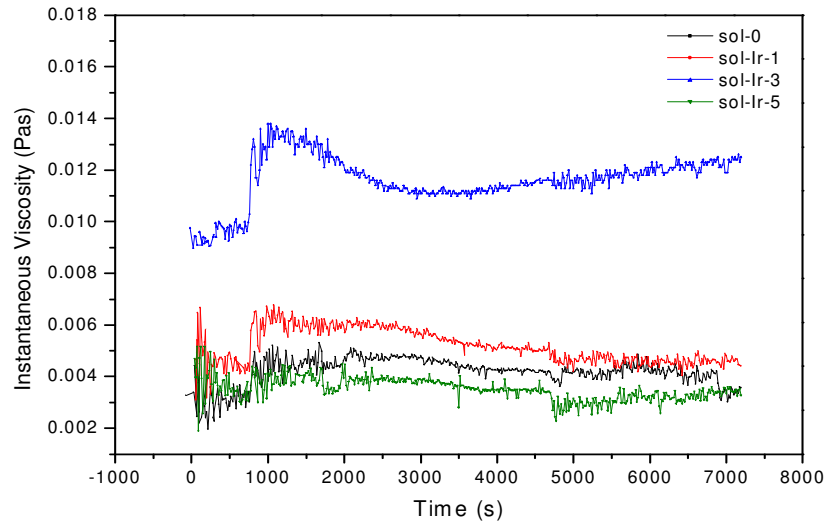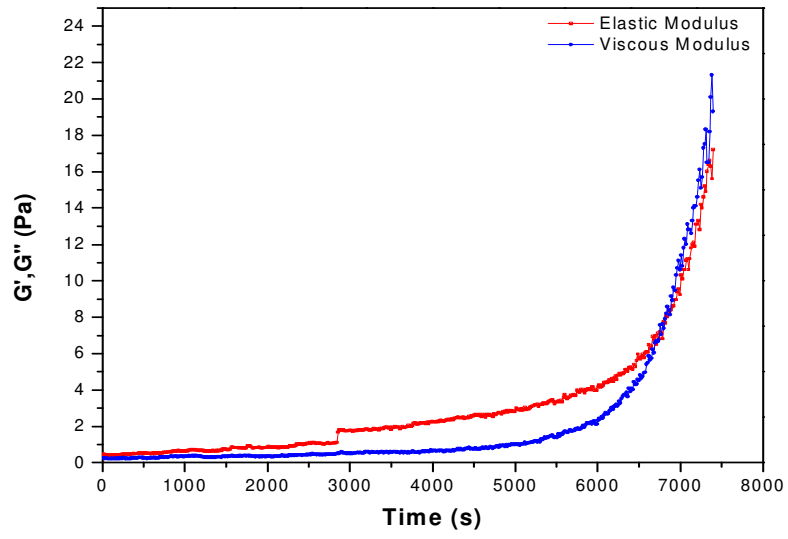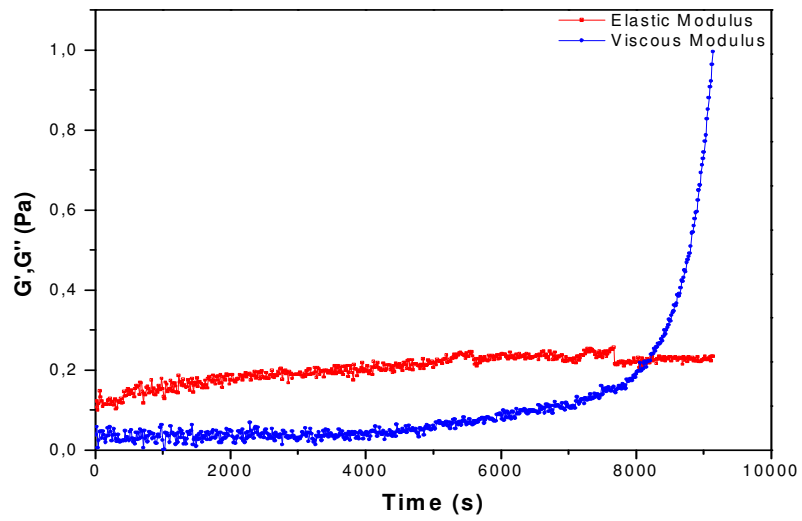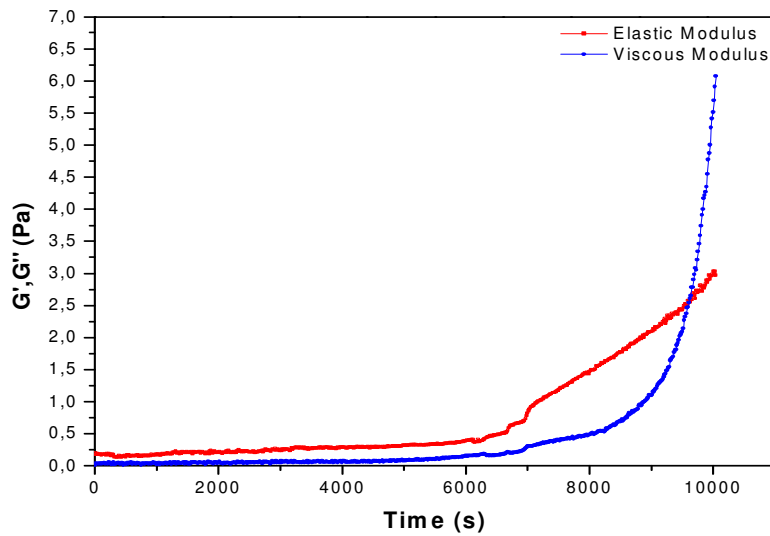

(a)
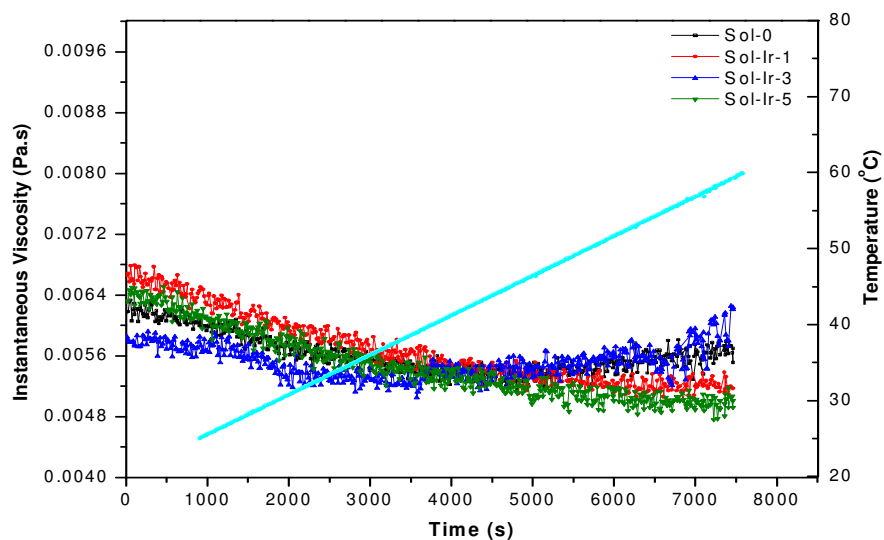
(b)

Figure 5.2 Viscosity measurement of undoped and BIO doped YBCO solutions (a) at room temperature and increasing shear rate and (b) at increasing temperature (25-60°C) and constant shear rate.

(a)

(b)

(c)

Figure 5.3 Modulus measurements of (a) undoped, (b) 5mole% BHO and (c) 5mole% BIO doped solutions.

5.1.2 Wettability Behaviors

After determination of rheological properties, contact angle value of all YBCO based precursor solutions on STO substrate was measured. Figure 5.4 shows the measurement of contact angle. It was found that the average contact angle values are $35.05°$, $31.71°$ and $25.50°$ for S-0, S-Hf-3 and S-Ir-3 respectively. These results indicated that good wettability can be expected from coating solutions for STO substrate in thin film production. As mentioned before, surface film quality is influenced by these by these contact angles. Since a very small wetting angle close to $0°$ was required in real applications, the obtained results provide a complete homogenous coverage on the STO single crystal substrates.
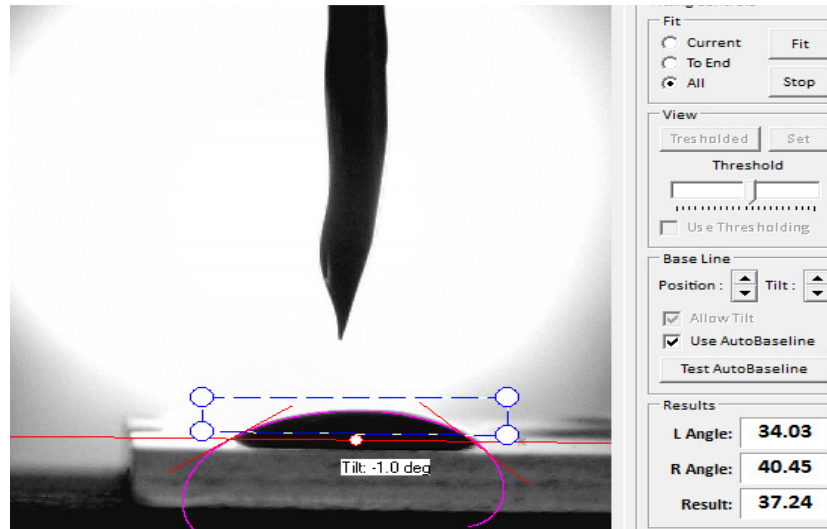
Figure 5.4 Wettability of undoped YBCO solution.

5.2 Material Characterization

5.2.1 Thermal Analysis

In production of homogeneous, crack-free, well-textured and high quality thin films, the pyrolysis stage is very important. During pyrolysis process, the vaporization of water and organic solvents and combustion of organic complexes may deteriorate the structures and superconducting properties of the thin films. Therefore before heat treatment process, undoped, Hf and Ir added YBCO precursor solutions were dried at 100^oC for 3 hours in air and consequently DTA/TG analysis performed under N_2 atmosphere. Figures 5.5 and 5.6 show the DTA/TG curves of YBCO based xerogels.

Llordes et al. (2010) divided this DTA/TG curves into three different stages. These stages are depicted in figure 5.7. They explained these stages like that: the first stage (stage I) involves both dehydration and evaporation of organic solvents, in the second stage (stage II); the thermolysis of coordinated solvents occurs. A fast weight loss (between 240^oC and 340^oC) occurs at this stage. Finally, the thermooxidative decomposition of TFAs comprises the third stage (stage III). Zhao et al. (2003) explained that at lower temperatures than 240^oC, organic solvent and water confined

to gel films runs out, which was clarified from a slow weight loss in TGA curves. It can be seen from DTA curves that the TFA salts decompose undergoing exothermic reactions at temperatures between 240°C and 340°C.
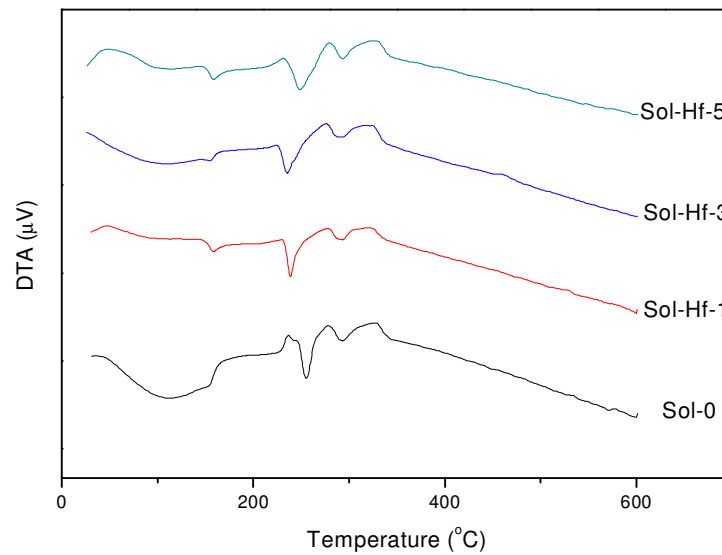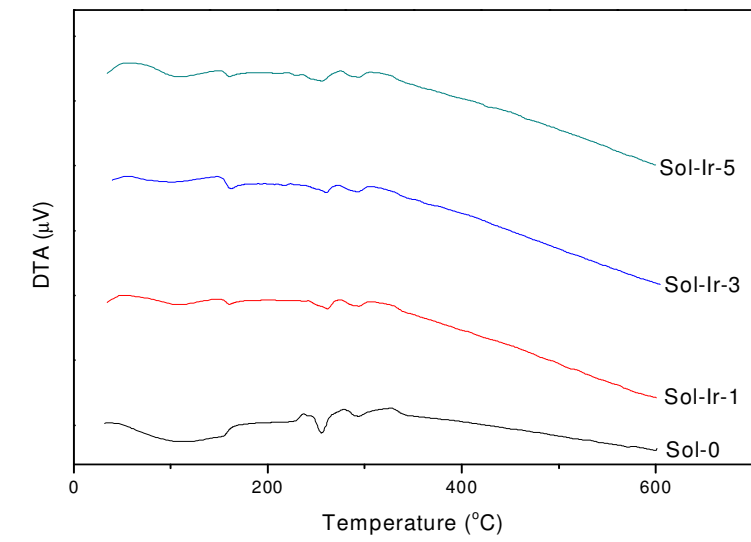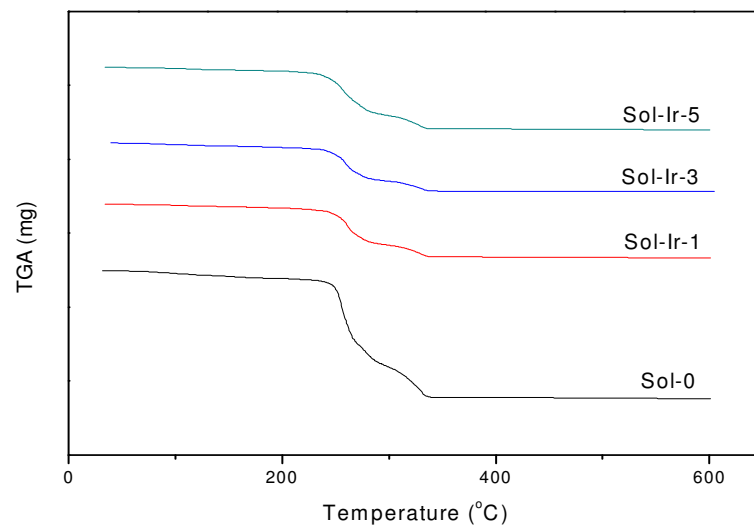

(a)
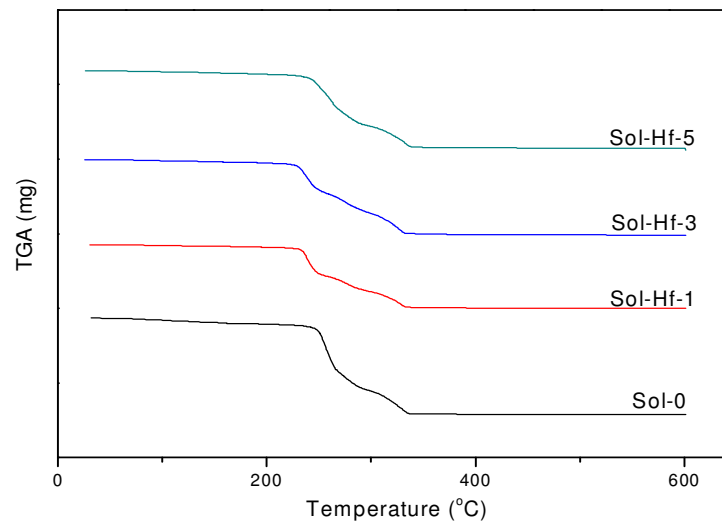
(b)

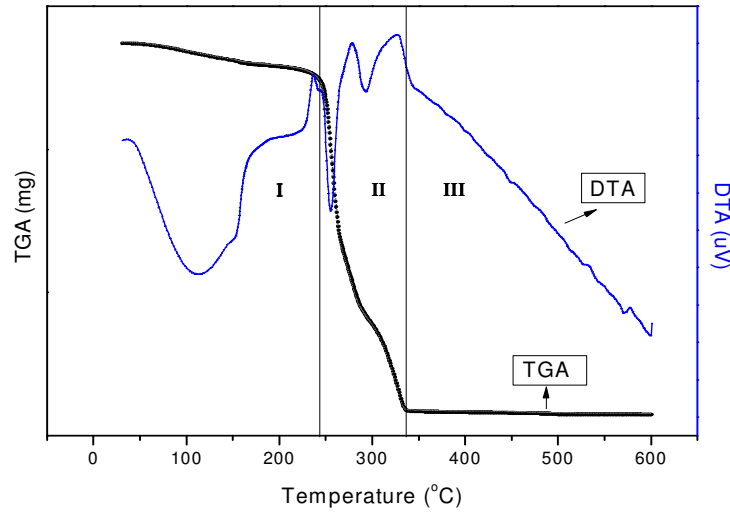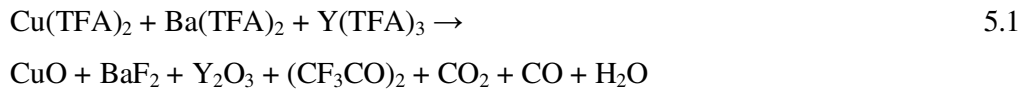Figure 5.5 (a) DTA and (b) TGA curves of undoped and BHO doped YBCO xerogels dried at 100°C for 3 hours in air.

(a)

(b)

Figure 5.6 (a) DTA and (b) TGA curves of undoped and BHO doped YBCO xerogels dried at 100°C for 3 hours in air.

Figure 5.7 DTA/TG curves of undoped YBCO xerogels dried at 100°C
for 3 hours in air.

Obradors et al. (2004) summerized reactions in two step, firstly calcination process will generate a homogeneous nanocrystalline film formed by CuO, Y$_2$O$_3$ and BaF$_2$, i.e. the decomposition reaction is,

$$Cu(TFA)_2 + Ba(TFA)_2 + Y(TFA)_3 \rightarrow \qquad \qquad 5.1$$
$$CuO + BaF_2 + Y_2O_3 + (CF_3CO)_2 + CO_2 + CO + H_2O$$

In a second step the metastable state created after the pyrolysis is heated to high temperatures ($\approx$700–800°C) under a controlled atmosphere and with a well determined temperature ramp. It has been suggested that the YBCO phase formation proceeds following the reaction,
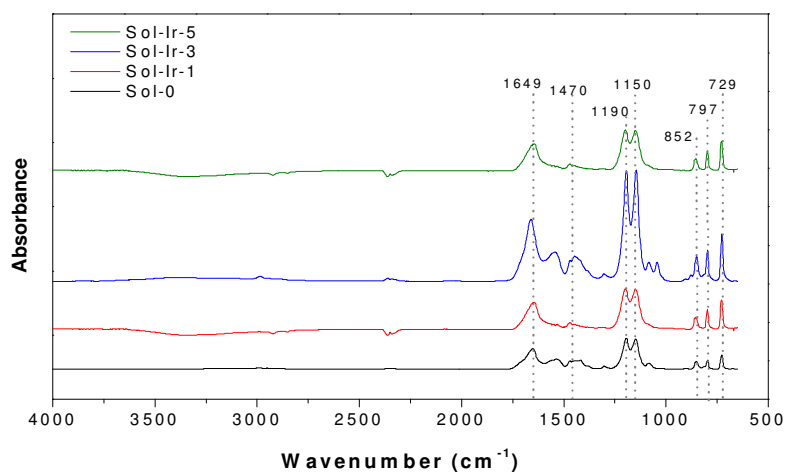
$$2BaF_2 + 2CuO + 1/2Y_2Cu_2O_5 + 2H_2O(g) \rightarrow \qquad \qquad 5.2$$
$$YBa_2Cu_3O_{6+x} + 4HF(g) + (1/2 - x)O_2(g)$$
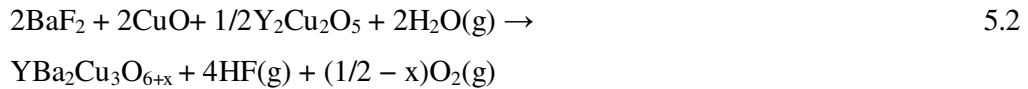
5.2.2 FT-IR Analysis

FTIR spectra of undoped and doped precursor powders which were dried at 100°C in air for 3 hours were shown in Figures 5.8 a and b.
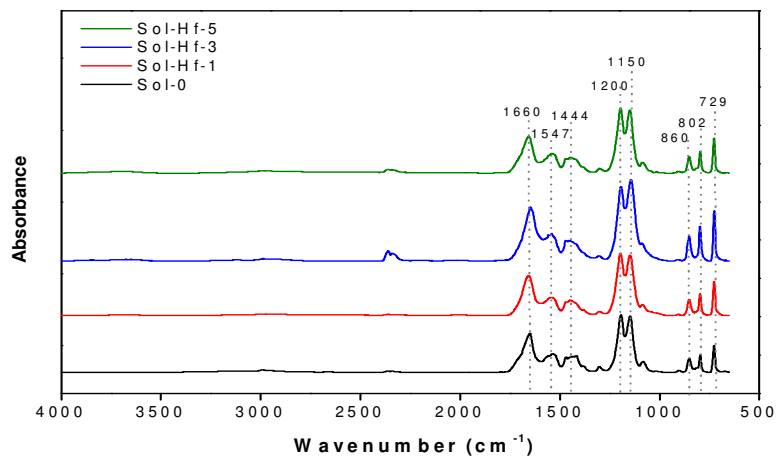
(a)

(b)

Figure 5.8 FTIR spectra of (a) doped and BHO doped (b) undoped and BIO doped YBCO powders dried at 100°C for 3 hours in air

It is obviously clear from Figure 5.8 that undoped, BHO and BIO doped solutions exhibited the same FTIR spectra. Bands at 2,365-2,345 cm^{-1} belong to carbon dioxide from the atmosphere and from the decomposition of the gel during heat

treatment process. It is interesting to note here that the acetate complexes started to decompose at $100^{\circ}C$ indicated by a change in intensity and to lower wave numbers as explained in the report of Thuy et al. (2009).

5.2.3 Phase Analysis

The θ-2θ diffraction patterns (Cu K_{α} radiation) of undoped and BHO doped YBCO films are shown in Figure 5.9. It was found that undoped and BHO doped films show strong YBCO peaks on STO substrates. The major peaks are (00l) and (l00) reflections of YBCO phase and STO substrate respectively. This behavior is quite likely to be a key feature for development of YBCO based superconducting films. These results also indicate that the YBCO films have highly c-axis texture. An unidentified and (110) YBCO peaks were also observed for undoped YBCO film. The main difference observed is an additional $BaHfO_3$ (002) peak in the Hf doped samples (Engel, Thersleff, Hühne, Schultz & Holzapfel, 2007). Araki, Yamagiwa & Hirabayashi (2001) have fabricated undoped YBCO thin films on STO substrate by similar method and obtained the same XRD patterns.

Figure 5.10 shows XRD patterns of undoped and BIO doped YBCO films. It was found that undoped and BIO doped films show strong YBCO peaks on STO substrates. As we presented in BIO doped YBCO films just before, the major peaks including (00l) and (l00) reflections of YBCO phase and STO substrate respectively can be seen from Figure 5.9. Here also the YBCO films possess highly c-axis texture. This signifies to be superconducting phase. Note that in this case that an additional $BaIrO_3$ (002) phase is present in the Ir doped YBCO samples.
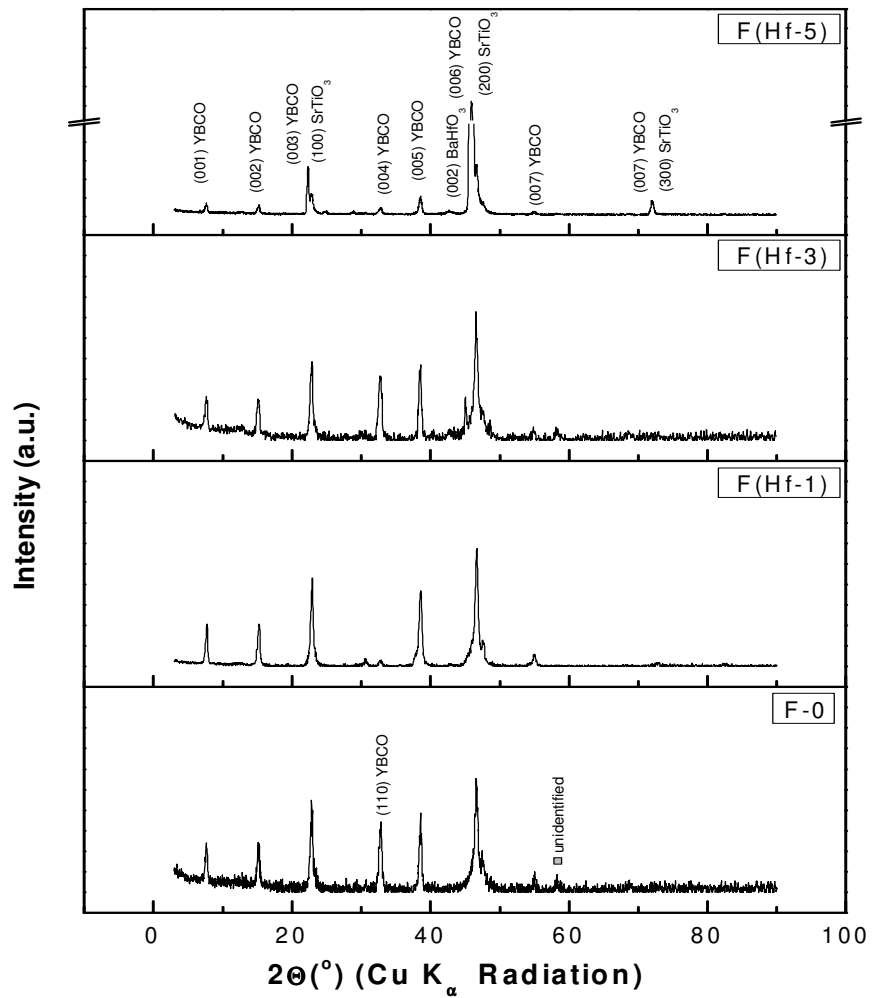
Figure 5.9 X-ray θ-2θ scans of superconducting samples including undoped and BaHfO$_3$ doped YBCO with a Cu Kα radiation. (YBCO JCPDS card no: 040-0159, STO JCPDS card no: 035-0734).

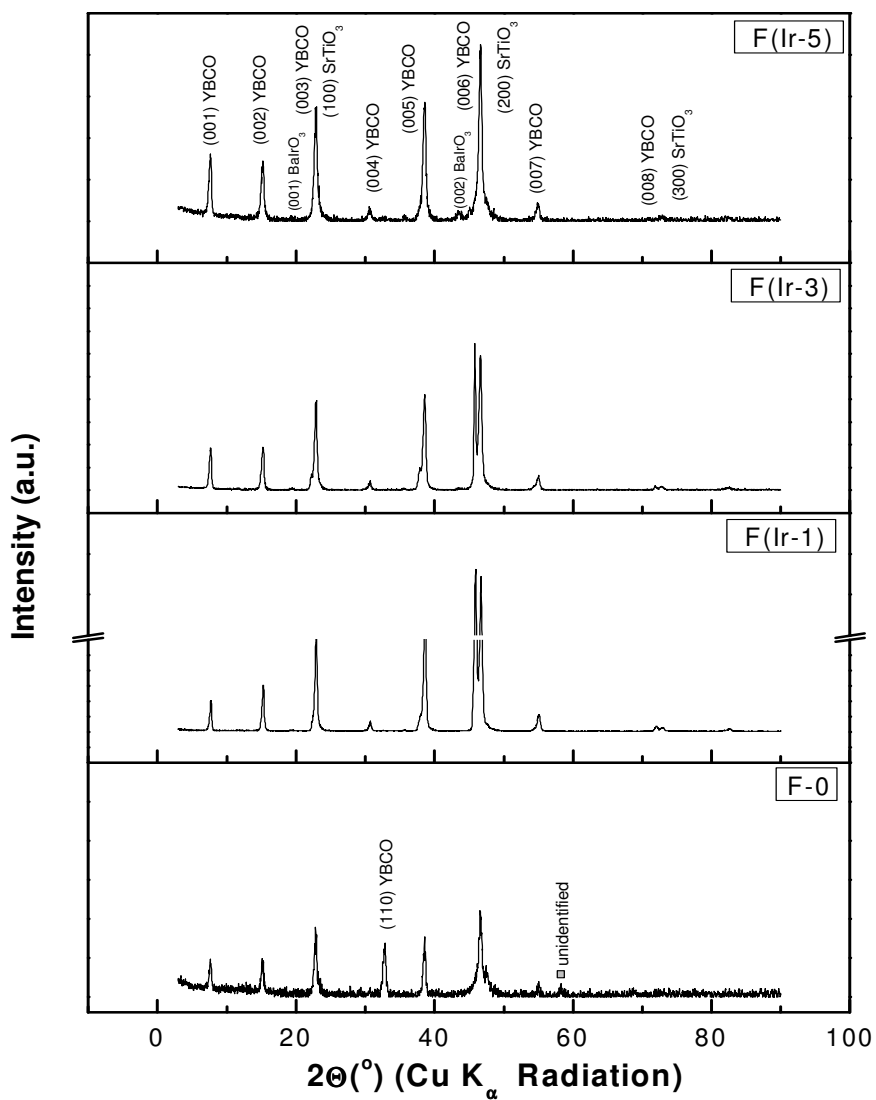Figure 5.10 X-ray θ-2θ scans of samples including undoped and BaIrO₃ doped YBCO with a Cu Kα radiation. (YBCO JCPDS card no: 040-0159, STO JCPDS card no: 035-0734).

5.2.4 XPS Analysis

Figure 5.11 shows a comparison of XPS survey scans of undoped and 3 mole% BHO and BIO doped YBCO thin films on STO single crystal substrates. It can be seen that the overall chemical compositions of all the films look very similar;

indicating that dopant materials such as Hf and Ir slightly affect overall chemistry of the films by virtue of their low contents in YBCO samples. It was found that C 1s peaks observed at 284 eV. Su, Joshi, Chintamaneni & Mukhopahyay explained that the component occurring at 291 eV is due to the –CF$_3$ group, whereas the one at 287.5 eV is because of –COOH. Note that after the calcining process these two components become very weak, indicating decomposition of the fluoroacetate group during calcination. The presence of other components of the C 1s peak, observed for the films both before and after calcination, can be attributed to C–O–R and/or the atmospheric contaminants absorbed during sample transfer. It should also be noted that no F 1s peaks observed.
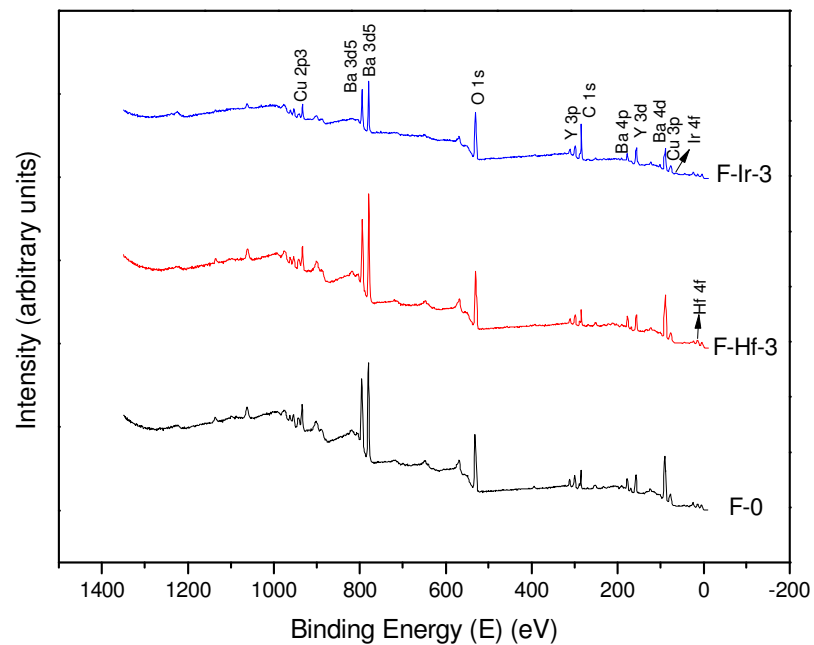

Figure 5.11 XPS survey scans for F-0, F(Hf-3) and F(Ir-3) thin films.

5.2.5 SEM-EDS Analysis

The surface morphologies of undoped and BHO doped YBCO film grown on STO substrate shown in Figure 5.12. All films have smooth and crack free surface. It should be noted that they generally have c-axis oriented grains, whilst their surface morphologies different from each other. Needle-like particulates represent a- or

b-axis oriented YBCO grains (Rufoloni et al., 2006). More importantly, these needle-like particulates increase with increasing BHO. In addition to these, 5 mole% BHO doped sample has porous surface and some needle shaped growth exists on the surface of the film.

(a)   (b)

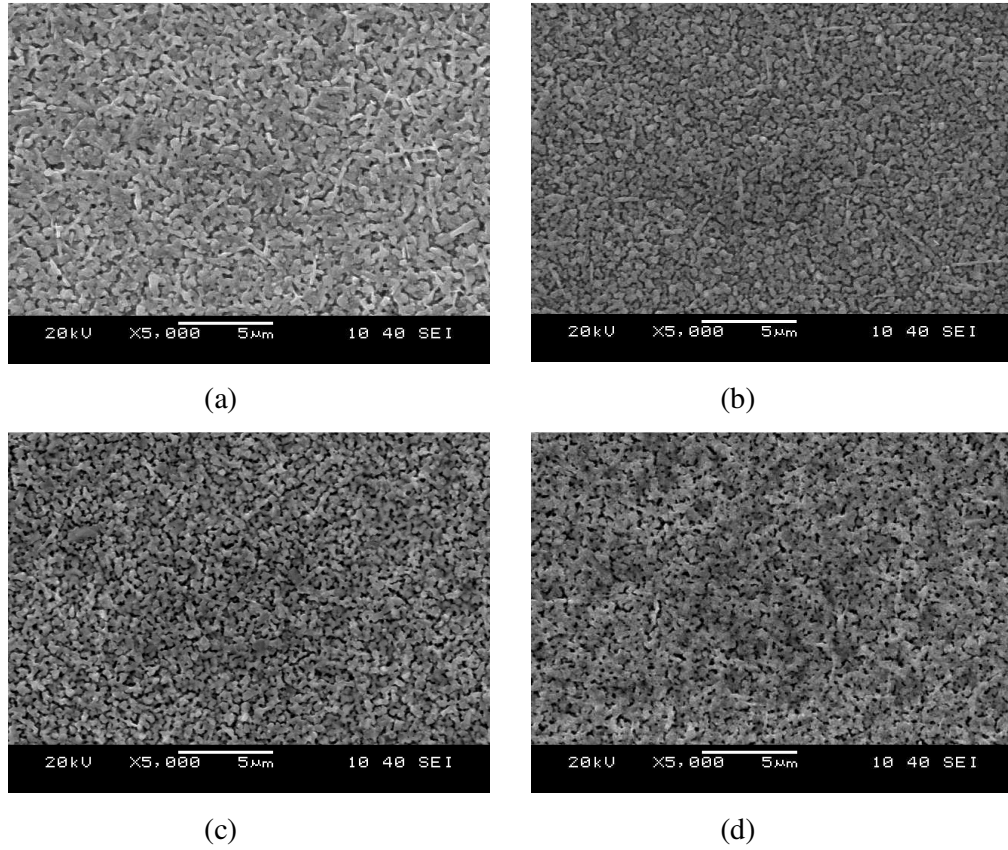(c)   (d)

Figure 5.12 SEM micrographs of pure and BHO doped YBCO films on STO substrates, including (a) F-0, (b) F (Hf-1), (c) F (Hf-3) and (d) F (Hf-5) samples.

The surface morphology of undoped and BIO doped YBCO thin films on STO substrates are presented in Figure 5.13, showing that all films have smooth and crack free surface like BHO doped samples. It is very important that these films generally have c-axis oriented for superconducting properties. As it can be seen from SEM pictures, undoped and 1 mole% doped YBCO films have some needle-shaped crystal structures, but for 3 and 5 mole% BIO doped YBCO films these needle-shaped particulates disappeared. Note that BIO doped YBCO films have small grain size compared with the undoped YBCO films.
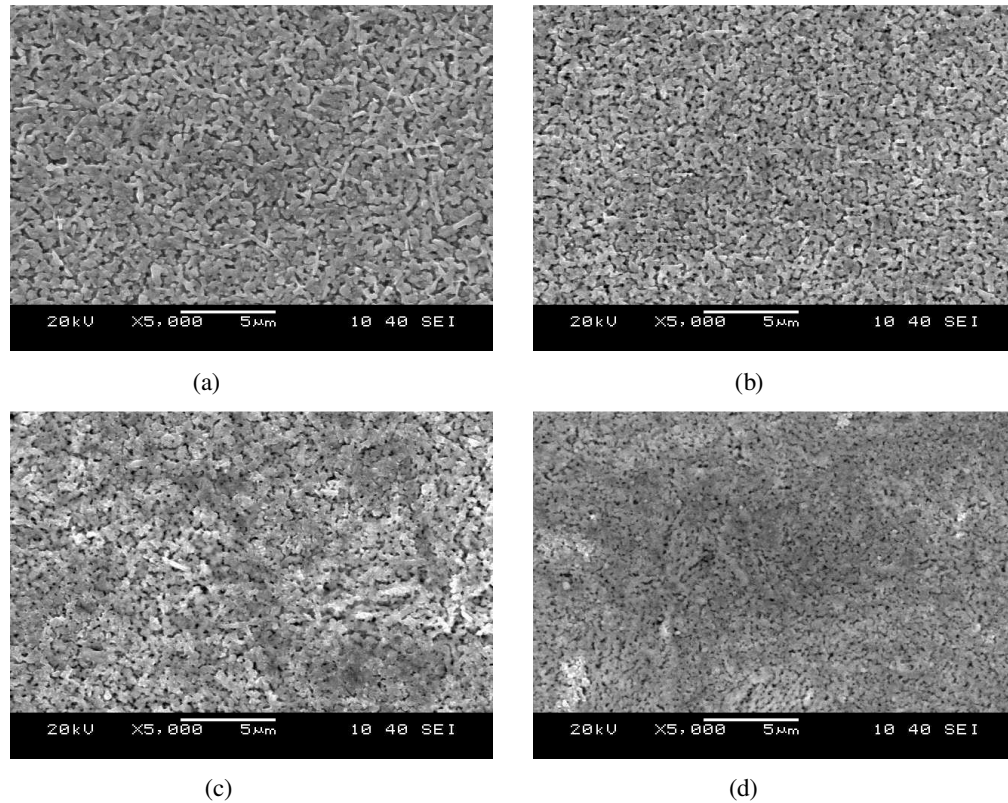
Figure 5.13 SEM micrographs of pure and BIO doped YBCO films on STO substrates, including, (a) F-0, (b)F (Ir-1), (c)F (Ir-3) and (d)F (Ir-5) samples

Elemental analysis and EDS spectra of undoped, 5 mole% BHO and BIO doped YBCO superconducting thin films deposited on STO single crystal substrate with the aid of TFA-MOD technique are illustrated in Figure 5.14 in detail. It can be seen clearly from the EDS spectrums that doped YBCO films contain Hf and Ir elements. It was proved that perovskite BHO and BIO nanoparticles with (100) separately formed in YBCO structure by only adding Hf and Ir precursors. It makes possible to form $BaHfO_3$ and $BaIrO_3$ perovskite structures by reacting Ba in YBCO structure. With Hf and Ir elements according to the following equations 5.3 and 5.4;

$$2Ba + 2Hf + 3O_2 \rightarrow 2BaHfO_3 \qquad\qquad 5.3$$
$$2Ba + 2Ir + 3O_2 \rightarrow 2BaIrO_3 \qquad\qquad 5.4$$

After these reactions $BaHfO_3$ and $BaIrO_3$ nano structures were easily formed as pinning centers in YBCO film on STO substrates. XRD results also supported them.

(a)

Component	Mole Conc.	Conc.	
Y	5.082	9.098	wt.%
Ba	2.210	6.110	wt.%
Sr	20.246	35.722	wt.%
O	37.259	12.004	wt.%
Ti	25.273	24.360	wt.%
Cu	9.930	12.706	wt.%
	100.000	100.000	wt.% Total

Elt.	Line	Intensity (c/s)	Error 2-sig	Conc	
O	Ka	15.44	0.786	12.004	wt.%
Ti	Ka	160.55	2.534	24.360	wt.%
Cu	Ka	31.33	1.119	12.706	wt.%
Sr	La	111.57	2.112	35.722	wt.%
Y	La	28.58	1.069	9.098	wt.%
Ba	La	9.30	0.610	6.110	wt.%
				100.000	wt.% Total

kV 20.0
Takeoff Angle 35.0°
Elapsed Livetime 100.0

(a)

(b)
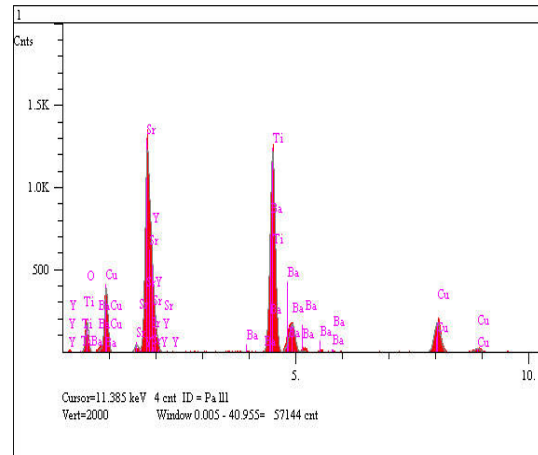
Component	Mole Conc.	Conc.	
Y	4.584	8.304	wt.%
Ba	2.016	5.640	wt.%
Sr	19.934	35.588	wt.%
Hf	0.019	0.070	wt.%
O	37.796	12.321	wt.%
Ti	25.302	24.677	wt.%
Cu	10.349	13.399	wt.%
	100.000	100.000	wt.% Total

Elt.	Line	Intensity (c/s)	Error 2-sig	Conc	
O	Ka	16.46	0.812	12.321	wt.%
Ti	Ka	169.22	2.602	24.677	wt.%
Cu	Ka	34.31	1.171	13.399	wt.%
Sr	La	115.23	2.147	35.588	wt.%
Y	La	27.05	1.040	8.304	wt.%
Ba	La	8.96	0.599	5.640	wt.%
Hf	La	0.04	0.041	0.070	wt.%
				100.000	wt.% Total

kV 20.0
Takeoff Angle 35.0°
Elapsed Livetime 100.0

(b)

(c)
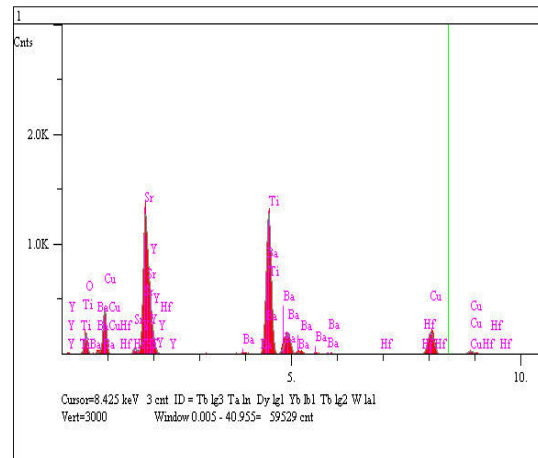
Component	Mole Conc.	Conc.	
Y	6.187	11.421	wt.%
Ba	0.809	2.308	wt.%
Sr	18.644	33.921	wt.%
Ir	0.604	2.413	wt.%
O	39.659	13.176	wt.%
Ti	25.271	25.117	wt.%
Cu	8.825	11.645	wt.%
	100.000	100.000	wt.% Total

Elt.	Line	Intensity (c/s)	Error 2-sig	Conc	
O	Ka	9.48	0.616	13.176	wt.%
Ti	Ka	94.99	1.949	25.117	wt.%
Cu	Ka	16.60	0.815	11.645	wt.%
Sr	La	63.49	1.594	33.921	wt.%
Y	La	21.43	0.926	11.421	wt.%
Ba	La	2.01	0.283	2.308	wt.%
Ir	La	0.56	0.149	2.413	wt.%
				100.000	wt.% Total

kV 20.0
Takeoff Angle 35.0°
Elapsed Livetime 100.0
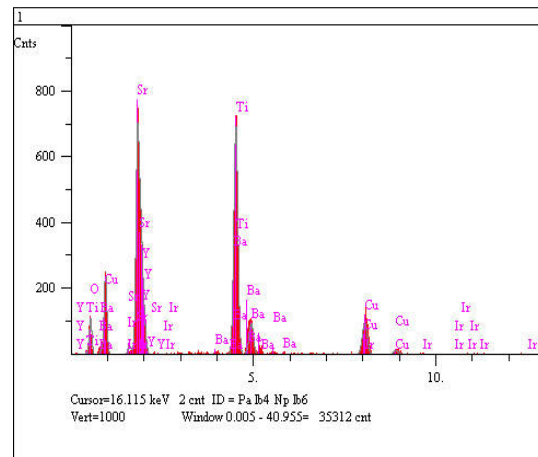
(c)

Figure 5.14 Elemental analysis and EDS spectra of (a) undoped, (b) 5% mole BHO doped, (c) 5% mole BIO doped YBCO films on STO substrates.

5.2.6 AFM Analysis

The surface morphologies of YBCO based samples are additionally characterized by means of AFM in order to determine surface roughness values of superconducting thin films. Figures 5.15, 5.16 and 5.17 depict 63.2 x 63,2 μm AFM 2D and 3D images of the surfaces of undoped, 3 mole% BHO and 3 mole% BIO added YBCO thin films on STO substrates. The average surface roughness (S_a) were 5.23 nm, 7.45 nm and 6.73 nm of F-0, F (Hf-3) and F (Ir-3) respectively.
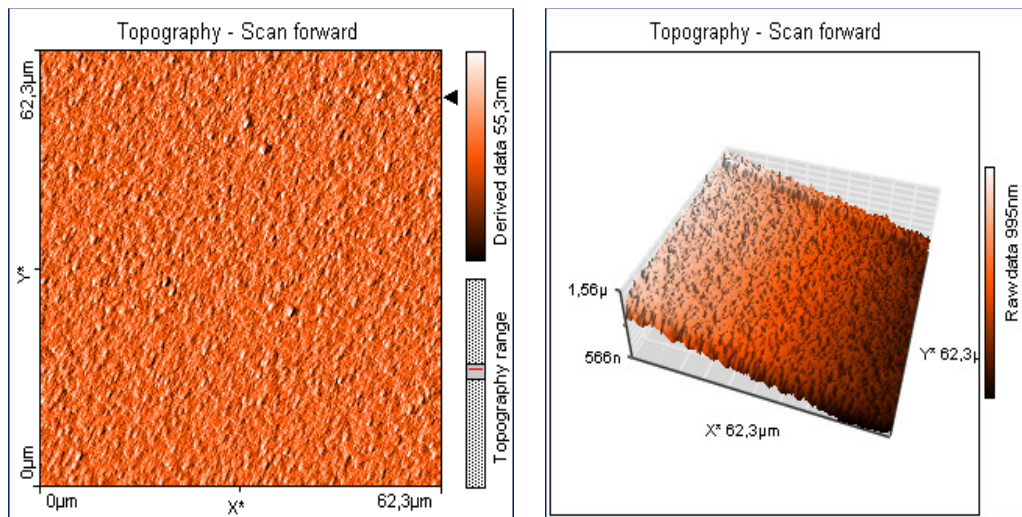

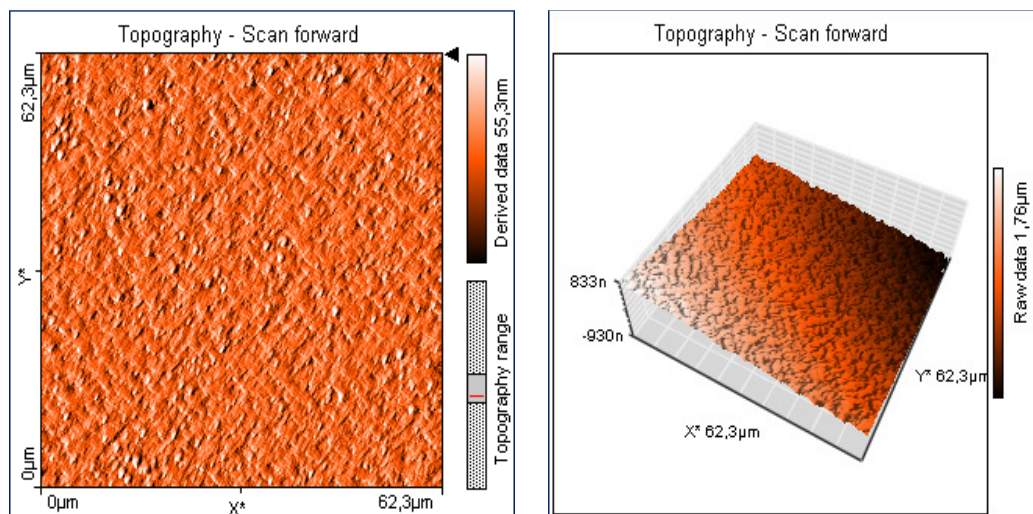Figure 5.15 AFM images of F-0 thin film on STO substrate.

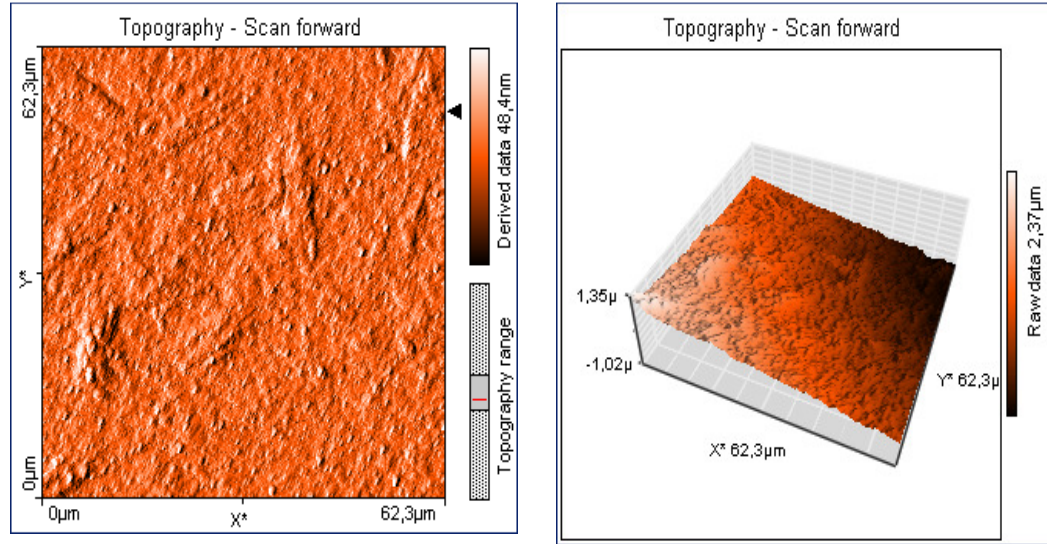Figure 5.16 AFM images of F (Hf-3) thin film on STO substrate.

Figure 5.17 AFM images of F (Ir-3) thin film on STO substrate.

Generally speaking, surface roughness is found to be in the range of 40 and 100 nm in solution based techniques. In our case, surface roughness values are much better than that of them. It can be stated out that surface quality of YBCO based films was improved very well.

5.2.7 Film Thickness

Determination of F-0, F-Hf-3 and F-Ir-3 thin film thickness is depicted in Figure 5.18, 5.19 and 5.20 respectively. Average film thickness value of YBCO samples is determined nearly 240 nm. Undoped and doped YBCO films have nearly same thickness values. Doping material does not affect the final film thickness.
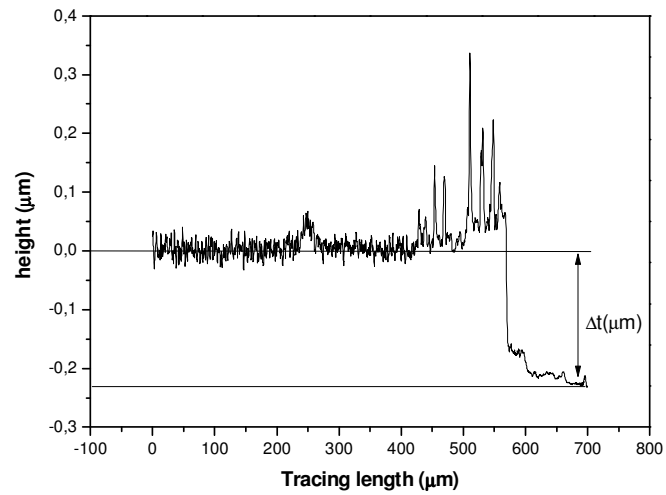
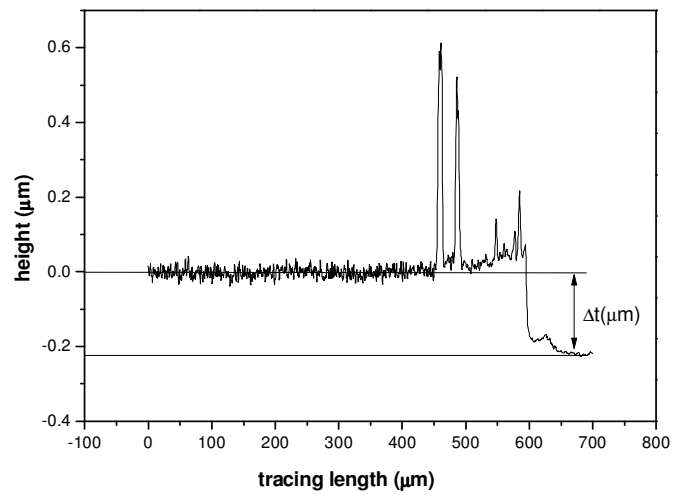Figure 5.18 Determination of film thickness F-0 thin film.

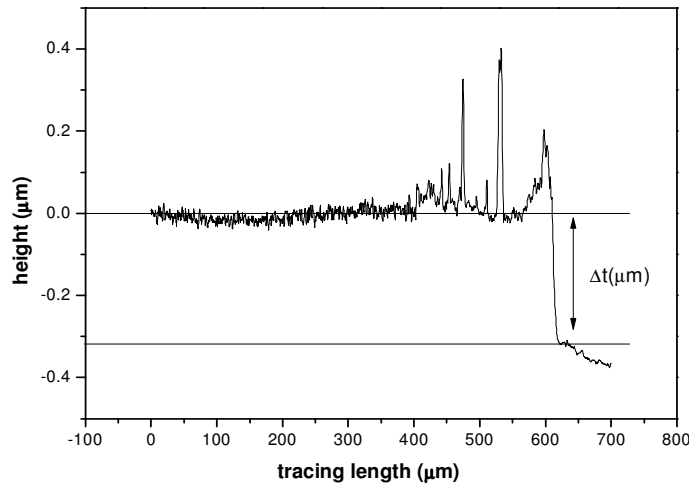Figure 5.19 Determination of film thickness F-Hf-3 thin film.

Figure 5.20 Determination of film thickness F-Ir-3 thin film.

5.2.8 Superconducting Properties

Figure 5.21 shows resistivity shift with temperature graph of undoped and BaIrO$_3$ added YBCO thin films. Undoped YBCO thin film has a high T$_c$ value (92K) but very large transition width (ΔT$_c$). It has not a sharp transition. In the case of transition width (ΔT$_c$), it is the measure of quality and homogeneity of the samples. The higher ΔT$_c$ is, the worst superconducting properties are. This means undoped YBCO film has include secondary phases. It can be exactly seen from the figure 5.21 that BIO doped YBCO thin films has high T_c (>91 K) and low ΔT$_c$ (around 1.5 K). All Ir added films have sharp transition. The inset graph has given to impress the effect of BaIrO$_3$. When BaIrO$_3$ concentration was increased from 1 mole% to 5 mole%, T_c value increased and ΔT$_c$ value decreased. 5 mole% Ir added film has the lowest ΔT$_c$. Critical current density versus magnetic field graph of undoped and Ir added films was shown in figure 5.22. Undoped YBCO film has bad J_c value under zero magnetic field like T_c because of the secondary phases in it. But when Ir concentration was increased J_c value increased under zero magnetic field and it reach 3.2 x 10^4 A/cm^2 with 3mol% Ir addition. With increasing magnetic field from 0 to 9 T, the critical current density values decreased very rapidly for all YBCO films. This J_c value is very low if we compare them with literature. Hänisch, Cai, Hühne,

Schultz & Holzapfel (2005) were performed a study with BaIrO$_3$ precipitates on YBCO thin films by PLD technique. They investigated its pinning properties. They also reach high J_c value like 3 x 10^6 A/cm^2. But they used bridges on thin films to carry out transport measurement.
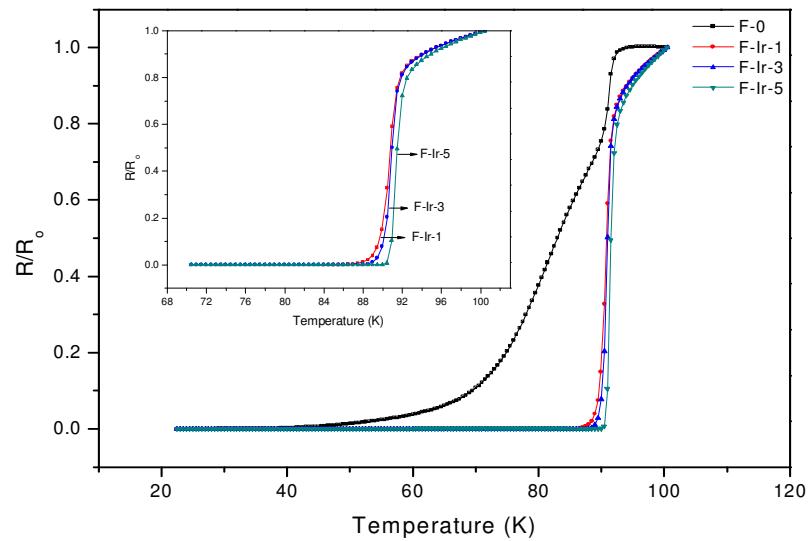

Figure 5.21 Resistance vs. temperature graph of Ir added YBCO thin films
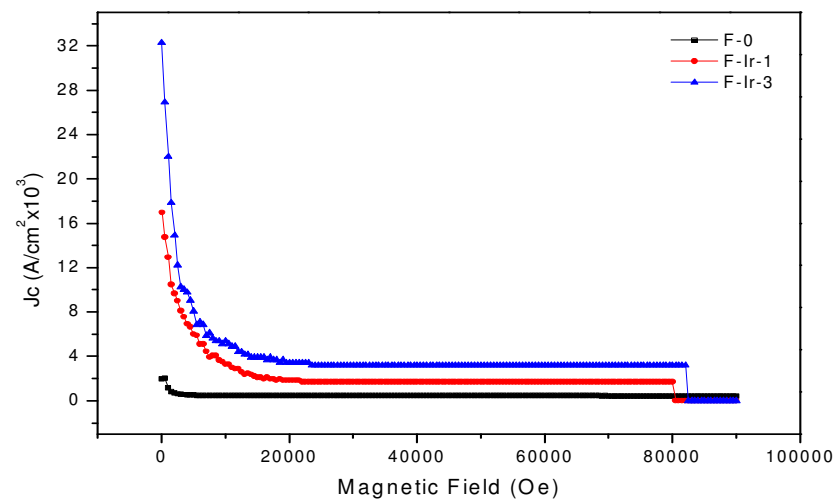

Figure 5.22 Critical current density vs. magnetic field graph of Ir added YBCO thin films

Resistivity shift with temperature graph of undoped and BaHfO$_3$ added YBCO thin films was depicted in figure 5.23. It is very clear from the graph that 1 mole% Hf addition straighten YBCO phase and the ΔT_c value getting smaller. With addition of 3 mole% BaHfO$_3$ nanoparticle YBCO phase spoiled again. YBCO thin film lost its superconductivity with 5 mole% Hf concentration.
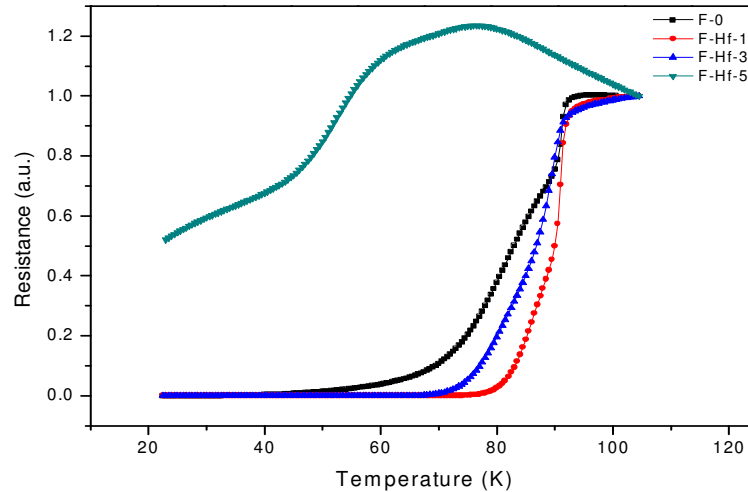

Figure 5.23 Resistance vs. temperature graph of Hf added YBCO thin films

Critical current density versus magnetic field graph of undoped and Hf added films was shown in figure 5.24. Critical current density was increased with the increasing Hf addition and it reaches 5×10^4 A/cm^2. This J_c value is also too low like BaIrO$_3$ nanoparticle doped YBCO films. Engel, Thersleff, Hühne, Schultz & Holzapfel (2007) studied the flux pinning properties of BaHfO$_3$ nanoparticle added YBCO thin film by TFA-MOD technique. They achieved nearly 3×10^6 A/cm^2 for Hf added YBCO films. As mentioned before that measurement technique is a very important issue here. In addition, precursor solution and heat treatment process can affect final film properties.
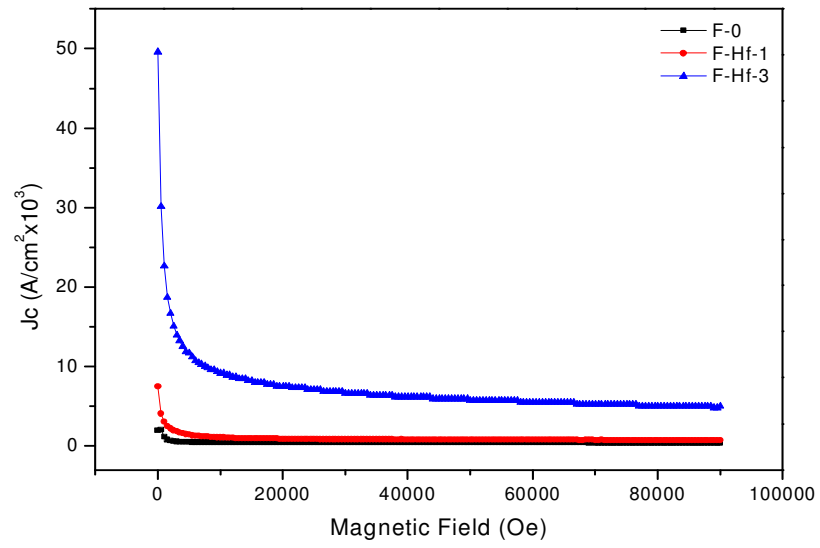
Figure 5.24 Critical current density vs. magnetic field graph of Ir added YBCO thin films

CHAPTER SIX
CONCLUSION AND FUTURE PLANS

In this study, production and characterization of undoped, BHO and BIO doped YBCO superconductor thin films on STO substrates were investigated by using TFA-MOD technique. Acetate base precursor chemicals were used to produce thin film.

Firstly solution characterization was performed. Contact angle and rheological properties of undoped and doped precursor solutions were investigated. Contact angle value of the undoped YBCO solution on STO substrate was measured as $35.05°$, and this value lower than $90°$, therefore these solutions can wet the single crystal substrates. Rheological characterization was performed to determine shear profile and effect of temperature on viscosity. For all solutions, at first viscosity value decreases with increasing temperature, but then they reach a constant value. Under increasing temperature conditions, undoped and doped YBCO solutions are Newtonian materials and their viscosity only depend on the temperature.

To determine heat treatment regime DTA-TG characterization were performed. At lower temperature ($<240°C$), organic solvent and water confined to gel films runs out, which was clarified from a slow weight loss in TGA curves. The TFA salts decompose which are exothermic reactions at temperature between $240-340°C$. At the same time fast weight losses between $240-340°C$ can be seen from the all TGA curves.

The phase structure of YBCO thin films was determined by XRD. In XRD patterns, generally the major peaks correspond to the (00l) reflections of the YBCO phases and (100) STO substrate which indicates that the films have a strong c-axis texture. Unfortunately undoped YBCO thin film includes some secondary phase at the same fabrication conditions.

In order to measure the chemical or electronic state of surface elements XPS was used. The overall chemical compositions of all the films look very similar and it should be noted that doping does not affect overall chemistry of the films.

SEM and AFM were used to identify surface morphologies of YBCO thin films on single crystal STO substrates. In general speak the surface morphologies of all samples have continuous, flat and crack free surfaces. However some a-axis oriented grains is observed for F-0. For BIO doped YBCO films present a denser surface structure compared with the undoped YBCO films.

Average film thickness value of YBCO samples is determined nearly 240nm.

The critical transition temperature, critical current density and critical magnetic field of samples were determined by using PPMS device. Standard four probe technique with silver paste contacts was used. Undoped YBCO film shows bad superconducting properties due to the secondary phases. In general speak, high T_c and low ΔT_c values were obtained for all Ir added YBCO thin films. J_c value also increased with $BaIrO_3$ nanoparticle addition under magnetic field. The pinning effect was observed with Ir addition. $BaHfO_3$ nanoparticle addition has also affected the YBCO superconducting properties. 5mole% Hf addition does not show superconductivity. The critical current density was increased with increasing Hf concentration.

It is recommended that acetate base precursor chemicals are more expensive than commercially available YBCO powder. Therefore to produce cheaper films, BHO and BIO doped precursor solutions can be prepared by using YBCO powder. To decrease a- or b-axis grains and increase surface morphology of final thin films, barium poor precursor solutions can be prepared. Determination of superconducting properties of thin films is very important issue. Standard four probe method with silver paste contact does not give accurate results. To reach high critical current density at high magnetic fields, bridges have to be patterned on films by using lithography devices and very small areas have to be used.

REFERENCES

Ahmed, W. & Jackson, M. (2009). *Emerging nanotechnologies for manufacturing.* USA: Elsevier.

Anthony, R. W. (2001). *Basic solid state chemistry (2nd Edition).* London: Willey.

Apetrii, C. (2009). *$YBa_2Cu_3O_{7-x}$ thin films prepared by chemical solution deposition.* Technical University of Dresden, Faculty of Mathematic and Natural Sciences, PhD Thesis.

Araki, T. & Hirabayashi, I. (2003). Review of a chemical approach to $YBa_2Cu_3O_{7-x}$ coated superconductors-metal organic deposition using trifluoroacetates. *Superconductor Science and Technology, 16,* 71–94.

Araki, T., Yamagiwa, K. & Hirabayashi I. (2001). Fabrication of $YBa_2Cu_3O_{7-x}$ film by metalorganic deposition method using trifluoroacetates and its process conditions. *Cryogenics 41,* 675-681.

Attia, S. M., Wang, J., Wu, G., Shen, J. & Ma, J. (2002). Rewiev on sol-gel derived coatings: process, techniques and optical applications. *Journal of Material Science Technology, 18,* 211-218.

Aytug, T., Paranthaman, M., Specht, E., Zhang, Y., Kim, K., Zuev, Y. et al. (2010). Enhanced flux pinning in MOCVD-YBCO through Zr additions: systematic feasibility studied. *Superconductor Science and Technology, 23,* 014005.

Bhuiyan, M.S., Paranthaman, M. & Salama, K. (2006). Solution-derived textured oxide thin films-a review. *Superconductivity Science of Technology,* 19, R1–R21.

Birlik, I. (2011). *Synthesis of superconducting films and improvement of their flux pinning properties with BaZrO₃ nanoparticles using chemical solution deposition method.* Dokuz Eylül University, The Graduate School of Applied and Natural Sciences, PhD Thesis.

Birlik, I., Erbe, M., Freudenberg, T., Celik, E., Schultz, L. & Holzapfel, B. (2010). Flux pinning improvement of YBCO superconducting films with $BaZrO_3$ nanoparticles prepared by chemical solution deposition method. *Journal of Physics Conference Series, 234,* 012004.

Callister, W. D. (2007). *Materials science and engineering - An Introduction* (7th ed.). United States of America: John Willey & Sons.

Campanini, D. (2011). *Contact Angle Measurements on Thin Films.* Retrieved July 1, 2012 from http:// www.desy.de/f/students/2011/reports/campanini.pdf.

Ekin, J. W. (2006). *Experimental techniques for low temperature measurements.* New York: Oxford University Press.

Engel, S., Thersleff, T., Hühne, R., Schultz, L. & Holzapfel, B. (2007). Enhanced flux pinning in $YBa_2Cu_3O_7$ layers by the formation of nanosized $BaHfO_3$ precipitates using the chemical deposition method. *Applied Physics Letters 90,* 102505.

Hänisch, J., Cai, C., Hühne, R., Schultz, L. & B. Holzapfel (2005). Formation of nanosized $BaIrO_3$ precipitates and their contribution to flux pinning in Ir-doped $YBa_2Cu_3O_{7-\delta}$ quasi-multilayers. *Applied Physics Letter, 86,* 122508.

Jha, A. K. & Khare, N. (2010). Investigation of flux pinning properties of $YBCO:BaZrO_3$ composite superconductor from temperature dependent magnetization studies. *Journal of Magnetism and Magnetic Materials, 322,* 2653–2657.

Kayatekin, I. (2006). *Synthesis and characterization of buffer layers and YBa$_2$Cu$_3$O$_x$ superconducting coatings by chemical solution deposition method.* Dokuz Eylül University, The Graduate School of Applied and Natural Sciences, MsSc Thesis.

Knoth, K., Engel, S., Apetrii, C., Falter, M., Schlobach, B., Hühne, R., et al. (2007). Chemical solution deposition of YBa$_2$Cu$_3$O$_{7-x}$ coated conductors. *Current Opinion in Solid State and Materials Science, 10,* 205–216.

Llordes, A., Zalamova, K., Ricart, S., Palau, A., Pomar, A., Puig, T., et al. (2010). Evolution of metal-trifluoroacetate precursors in the thermal decomposition toward high-performance YBa$_2$Cu$_3$O$_7$ superconducting films. *Chemistry of Materials 2010, 22,* 1686–1694.

Murase, S., Itoh, K., Wada, H., Noto, K., Kimura, Y., Tanaka, Y. et al. (2001). Critical temperature measurement method of composite superconductors. *Physica C, 357-360,* 1197-1200.

Nakaoka, K., Matsuda, J., Kitoh, Y., Goto, T., Yamada, Y., Izumi, T., et al. (2007). Influence of starting solution composition on superconducting properties of YBCO coated conductors by advanced TFA-MOD process. *Physica C, 463–465,* 519-522.

Nakaoka, K., Ichikawa, H., Miura, M., Sutoh, Y., Yoshizumi, M., Izumi, T., Yamada, Y., et al. (2009). Investigation on starting solution of TFA-MOD process for high speed production of YBCO coated conductors. *Physica C, 469,* 1326–1328.

Obradors, X., Puig, T., Pomar, A., Sandiumenge, F., Pinol, S., Mestres, N., et al. (2004). Chemical solution deposition: a path towards low cost coated conductors. *Superconductor Science and Technology, 17,* 1055–1064.

Owens, F. J. & Poole, C. P. (1996). *The new superconductors*. New York: Plenum Press.

Overview of Application (n.d.). Retrieved January 20, 2012 from http://www.ccas-web.org/superconductivity/overview/.

Poole, C. P., Farach, H., Creswick, R. J. & Prozorov R. (2007). *Superconductivity, (2nd edition).* Amsderdam: Elsevier.

Ramachandran, V.S., Paroli, R. M., Beaudoin, J., & Delgado, A. H. (2002). *Handbook of Thermal Analysis of Construction Materials.* USA: Noyes Publications.

Roma, N., Morlens, S., Ricart, S., Zalamova, K., Moreto, J. & Pomar, A. (2006). Acid anhydrides: a simple route to highly pure organometallic solutions for superconducting films. *Superconductor science and technology 19*, 521-527.

Rufoloni,A., Augieri, A., Celentano, G., Galluzzi, V., Mancini A., Vannozzi, A. et al. (2006). $YBa_2Cu_3O_{7-x}$ films prepared by TFA-MOD method for coated conductor application. *Journal of Physics Conference Series 43,* 199–202.

Sarrao et al., (2006). Report of the basic energy sciences workshop on superconductivity. *USDOE Office of Science, 899129.*

Schwartz, R. W. (1997). Chemical solution deposition of perovskite thin films. *Chemistry of Materials 9,* 2325-2340.

Sheahen P. T. (2002). *Introduction to High-Temperature Superconductivity.* New York, Boston, Dordrecht, London, Moscow: Kluwer Academic Publishers.

Su, J., Joshi, P., Chintamaneni, V. & Mukhopadhyay, M. (2005). The influence of the heating rate on YBCO films prepared by the trifluoroacetates metal-organic deposition process. *Superconductor Science and Technology, 18*, 1496-1501.

Thermo Nicolet Corporation, (2001*). Introduction to fourier transform infrared spectrometry*. Retrieved July 15, 2012 from http://mmrc.caltech.edu/FTIR/FTIRintro.pdf.

Thuy, T., Hoste, S., Herman, G., Buysser, K., Lommens, P., Feys, J. et al, (2009). Sol-gel chemistry of an aqueous precursor solution for YBCO thin films. *Sol gel Science and Technology 52*, 124-133.

Winter, H. H. (1987). Can the gel point of a cross-linking polymer be detected by the G´-G´´ crossover?. *Polymer engineering and science 27 (22),* 1698-1702.

Vandaele, K. (2011). *YBa$_2$Cu$_3$O$_7$ coatings based on trifluoro-acetic acid precursors.* University of Cambridge: M.Sc Thesis.

Zhao, B., Sun, Z.Y., Shi, K., Yang, J., Sun, Y.P. & Han, Z.H. (2003). Preparation of YBa$_2$Cu$_3$O$_{7-d}$ films by MOD method using trifluoroacetate as precursor. *Physica C, 386,* 342–347.